

Unifying the dynamical classification of early-type galaxies: kinematic deficits in IllustrisTNG versus observations

Wenyu Zhong¹, Min Du¹*, Shengdong Lu², Yunpeng Jin³, and Kai Zhu³

¹ Department of Astronomy, Xiamen University, Xiamen, Fujian 361005, China

² Institute for Computational Cosmology, Department of Physics, University of Durham, South Road, Durham, DH1 3LE, UK

³ Department of Astronomy, Westlake University, Hangzhou, Zhejiang 310030, China

Received 2025/09/19; accepted 2026/01/30

ABSTRACT

Aims. This study aims to make a comparative analysis of galaxy kinematics using IllustrisTNG simulations and integral-field spectroscopy (IFS) observations.

Methods. We identify 2,342 early-type galaxies (ETGs) from the TNG100 simulation and 236 ETGs from the TNG50 simulation to compare with those from MaNGA and ATLAS^{3D} surveys. For these systems, we measure key kinematic parameters widely employed in both observational and simulation-based studies, including the intrinsic spin parameter $\lambda_{R,\text{intr}}$ (it indicates that the λ_R parameter is measured when the galaxy is viewed edge-on), the cylindrical rotational energy fraction κ_{rot} , and structural mass ratios such as the spheroid mass fraction f_{spheroid} and the stellar halo mass fraction f_{halo} .

Results. This study performs a comparative kinematic analysis of early-type galaxies using IllustrisTNG simulations and IFS data from MaNGA and ATLAS^{3D}. We demonstrate that standard classifiers—the $\lambda_R(R_e) = 0.31\sqrt{\varepsilon}$ relation and \bar{k}_5 coefficient (the higher-order term of the Fourier decomposition of velocity fields)—fail to align with kinematic bimodality. Revised thresholds are proposed: the spin $\lambda_{R,\text{intr}} \sim 0.4$, the ratio of rotation energy $\kappa_{\text{rot}} \sim 0.5$, and the mass fraction of a spheroid component $f_{\text{spheroid}} \sim 0.6$. It provides a universal threshold that classifies all kinds of galaxies into rotation-dominated (fast rotators) and random motion-dominated (slow rotators) cases. Scaling relations derived from TNG enable estimation of κ_{rot} and f_{spheroid} from observations. TNG simulations exhibit a bimodality deficit, characterized by a lack of fast rotators and suppressed $\lambda_{R,\text{intr}}$, attributable to excess galaxies with intermediate rotation and high spheroid/stellar halo mass. A novel method for estimating stellar halo mass fractions from IFS kinematics is introduced, though significant uncertainties persist.

Key words. galaxies: fundamental parameters – galaxies: elliptical and lenticular – galaxies: structure – galaxies: kinematics and dynamics – galaxies: halos

1. Introduction

The consensus holds that early-type galaxies (ETGs) are generally quiescent systems that underwent early cessation of star formation, resulting in their current red optical colors and minimal reserves of cold gas and dust (van den Bergh 1999). Morphologically, ETGs appear symmetric and predominantly elliptical, with shapes ranging from near-circular to highly elongated (Sandage 2005). Classified within Hubble's framework (Hubble 1926, 1936), ETGs comprise two main types, i.e., elliptical and lenticular (S0) galaxies. Elliptical galaxies are smooth tri-axial ellipsoids devoid of spiral arms or nebulae. Their surface brightness follows de Vaucouleurs' law (de Vaucouleurs 1948), featuring concentrated central peaks and sharp outward declines (Kormendy 1977). Lenticular galaxies retain disk-like structures but lack spiral arms, often exhibiting central bars or rings (e.g., Sandage et al. 1970; van den Bergh 1976; Graham & Guzmán 2003).

Integral Field Spectroscopy (IFS) technology enables the classification of dust-unaffected ETGs into “Fast Rotators (FRs)” and “Slow Rotators (SRs)” based on projected kinematic properties (Emsellem et al. 2004, 2007, 2011). This division originated from qualitative observations in the SAURON sur-

vey of 48 ETGs (Emsellem et al. 2004), which revealed a dichotomy: galaxies exhibited either regular rotation patterns or complex/irregular stellar velocity maps, and are defined as regular rotators (RR)/non-regular rotators (NRR). Quantification of kinematic regularity is achieved through harmonic term analysis (e.g., the higher-order term of the Fourier decomposition of velocity fields k_5 (Krajnović et al. 2006, 2008), see details in Section 4), distinguishing regular rotators from non-regular rotators (Krajnović et al. 2011; Cappellari 2016). The correspondence between RR/FR and NRR/SR led to the adoption of the spin parameter λ_R (Emsellem et al. 2011, 2007), with SRs defined by $\lambda_R < 0.31\sqrt{\varepsilon}$ within the effective radius R_e , where ε is the ellipticity. FRs display high λ_R and ε , resembling disk galaxies, while SRs feature weak rotation ($\lambda_R \lesssim 0.15$). IFS surveys like SAURON (de Zeeuw et al. 2002), ATLAS^{3D} (Cappellari et al. 2011a), CALIFA (Sánchez et al. 2012), SAMI (Croom et al. 2012; Bryant et al. 2015), MASSIVE (Ma et al. 2014), and MaNGA (Bundy et al. 2015) provide spatially resolved kinematic maps, facilitating studies of ordered versus disordered motion via λ_R - ε diagnostics. However, the robustness of this classification has not been systematically examined in numerical simulations. And the correlation between \bar{k}_5 and other kinematic parameters, e.g., the relative importance of cylindrical rotation energy (Sales et al. 2010) that have been widely used in simulations, is poorly quantified.

* Min Du and Wenyu Zhong contribute equally to this work. Corr. author: Min Du (E-mail: dumin@xmu.edu.cn)

Recent cosmological hydrodynamical simulations, e.g., EAGLE (Schaye et al. 2015; Crain et al. 2015), IllustrisTNG (TNG hereafter, e.g., Nelson et al. 2018), Horizon-AGN (Dubois et al. 2014, 2016), New-Horizon (Dubois et al. 2021), Magneticum (Dolag et al. 2025), and SIMBA (Davé et al. 2019), have made remarkable progress that successfully reproduces realistic visual morphologies and properties in many aspects. These remarkable progresses allow statistical studies of galaxies in a fully self-consistent cosmological environment. On one hand, a systematic comparison between IFS results and kinematic properties in simulations is crucial for constraining the potential shortage of simulations. On the other hand, numerical simulations can be used to examine the kinematic models and classification of SRs and FRs. It must be pointed out that, in addition to being able to reproduce fairly well the morphological properties observed, modern cosmological hydrodynamic simulations – including the TNG suite – demonstrate a certain degree of reliability in reproducing the observed kinematic properties. Santucci et al. (2024) first established that the EAGLE simulation successfully models the stellar mass fraction variation across orbital families as functions of stellar mass and spin parameter at $z = 0$, consistent with SAMI observations. This alignment extends to the correlation between specific angular momentum j_* and stellar mass M_* , where Lagos et al. (2017) reported reasonable agreement between EAGLE results and ATLAS^{3D} data. Similarly, analyses of the Magneticum Pathfinder simulations reveal highly congruent $\lambda_R(R_e)$ and ε distributions for ETGs compared to ATLAS^{3D}, CALIFA, SAMI, and SLUGGS surveys (Schulze et al. 2018). Further validation by Schulze et al. (2020) confirms that Magneticum’s stellar spin parameter profiles closely match observations from SLUGGS (Arnold et al. 2014; Forbes et al. 2017) and ePN.S (Pulsoni et al. 2018). Building on CALIFA’s kinematic “Hubble sequence” derived from stellar orbit-circularity distributions, Xu et al. (2019) analyzed $z = 0$ TNG galaxies to explore connections between stellar orbital compositions and fundamental galaxy properties. They found TNG100 broadly reproduces observed orbital-component fractions and their stellar-mass dependencies. Similarly, Zhang et al. (2025) further presented that TNG galaxies match well with the luminosity fractions of cold, warm, and hot orbital components of CALIFA galaxies that are extracted via performing the orbit-superposition Schwarzschild modeling (e.g., Schwarzschild 1979; Valluri et al. 2004; van den Bosch et al. 2008; Zhu et al. 2018b,a,c). Moreover, IllustrisTNG have reproduced galaxies with unusual structural and kinematic properties, such as low surface brightness galaxies (Zhu et al. 2018d), and jellyfish galaxies (Yun et al. 2019). Therefore, to a certain extent, TNG simulations can be employed for further research on the kinematic parameters and properties of galaxies.

Structural mass ratios derived from kinematic decomposition and cylindrical rotational properties are able to characterize galaxy dynamical properties and their underlying formation histories. However, observational measurement of spins, κ_{rot} , and precise structural mass ratios are challenging. For simulations, kinematic phase-space analysis enables robust decomposition: the auto-GMM method, an unsupervised algorithm developed by Du et al. (2019), identifies structures such as cold disks, warm disks, bulges, and halos in TNG galaxies by clustering stellar particles in a 3D kinematic phase space of normalized azimuthal angular momentum (circularity), non-azimuthal angular momentum, and binding energy. Galaxies with minimal stellar halos exhibit tight scaling relations among j_* , M_* , size, and metallicity owing to their quiescent merger histories (Du et al. 2022, 2024; Ma et al. 2024). Despite the auto-GMM’s success in isolating intrinsic structures formed by distinct mecha-

nisms—such as separating stellar halos from bulges (Du et al. 2020, 2021)—the kinematic decomposition cannot be directly applied to observational datasets. Consequently, linking kinematically derived structures as well as galactic spin to IFS observables is critical. Moreover, while $\kappa_{\text{rot}} = 0.5$ or a spheroid mass ratio of 0.5 serves as a common threshold for classifying elliptical versus disk galaxies (e.g., Zhao et al. 2020; Fall & Rodriguez-Gomez 2023; Pérez-Montaño et al. 2024; Kataria & Vivek 2024), its relationship to kinematically distinct FRs and SRs in IFS surveys remains unclear.

In this paper, we perform a comparative analysis of galaxy kinematics using TNG simulations and IFS data from the MaNGA and ATLAS^{3D} surveys, with a focus on classifying early-type galaxies into FRs and SRs, as well as interpreting the definitions of FRs and SRs. The structure of this paper is organized as follows. Section 2 describes the ETGs sample selection and data extraction from IFS observations. Section 3 describes mock observations and sample selection of TNG simulation galaxies. Section 4 demonstrates the kinematic parameters quantifying rotation properties of galaxies. Section 5 investigates the relation between different kinematic parameters. Section 6 examines the bimodality and the classification of slow and fast rotators in kinematics. Section 7 compares the radial distribution of kinematic properties between TNG simulations and observations. Our conclusions are discussed and summarized in Sections 8 and 9, respectively.

2. Sample selection and data extraction from IFS observations

2.1. Data extraction of color, morphology, and rotation

This study compares the kinematic properties of simulated TNG galaxies with IFS measurements from the ATLAS^{3D} and MaNGA surveys for ETGs. ATLAS^{3D}¹ is a complete, multi-wavelength, volume-limited survey of nearby ETGs, and its final sample encompasses 260 nearby ETGs. The Sloan Digital Sky Survey-IV (SDSS-IV: York et al. 2000; Gunn et al. 2006; Blanton et al. 2017) Mapping Nearby Galaxies at Apache Point Observatory (MaNGA², Bundy et al. 2015; Yan et al. 2016) is an IFS survey designed to obtain spectral measurements across the surfaces of approximately 10,000 nearby galaxies. The data of color, morphology, and stellar mass of our sample are extracted as follows.

Color $g - r$ – The $g - r$ colors for MaNGA galaxies and most ATLAS^{3D} galaxies are obtained from the NASA-Sloan Atlas³ (NSA) catalog (Blanton & Roweis 2007; Blanton et al. 2011). For the subset of ATLAS^{3D} galaxies not included in the NSA catalog, we use $B - V$ colors corrected for Galactic extinction from the Hyperleda⁴ catalog (Makarov et al. 2014). These $B - V$ colors are then converted to $g - r$ colors using the relation provided in Pulsoni et al. (2020).

Size R_e – The effective radius R_e of the ATLAS^{3D} sample is adopted from the Table 1 in Cappellari et al. (2013b). The data of MaNGA is from Zhu et al. (2023). MaNGA provides spatially resolved spectra, covering radial ranges out to $1.5R_e$ for the Primary+ sample (about two-thirds of the total sample) and out to $2.5R_e$ for the Secondary sample (about one-third of the total sample).

¹ <http://www-astro.physics.ox.ac.uk/atlas3d/>

² <https://www.sdss4.org/surveys/manga>

³ <http://www.nsatlas.org>

⁴ <http://leda.univ-lyon1.fr/>

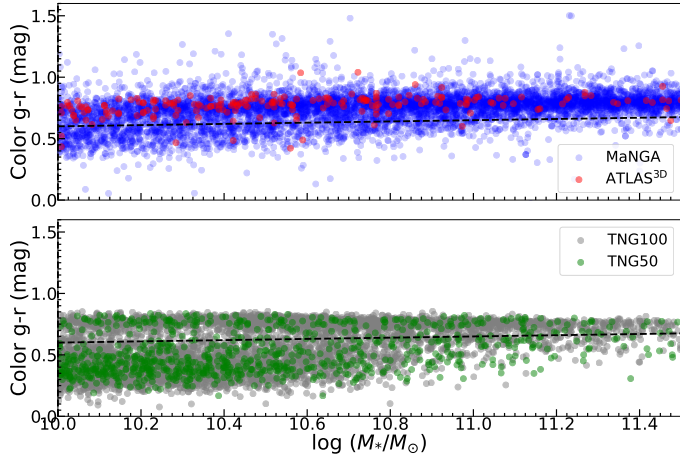


Fig. 1. The $g - r$ color-stellar mass diagram. The upper and lower panels of the figure display observational data (from MaNGA and ATLAS^{3D}) and simulated data (from TNG50 and TNG100), respectively, encompassing all samples within the mass range of $10^{10} - 10^{11.5} M_{\odot}$. Red sequence ETGs are selected above the dashed line.

Stellar mass M_* – The stellar masses for the ATLAS^{3D} and MaNGA sample are derived using a color–mass relation assuming the Chabrier (2003) initial mass function. For the ATLAS^{3D} dataset, total absolute K -band luminosities (L_K) are adopted directly from Cappellari et al. (2011a). For the MaNGA dataset, L_K values originate from Graham et al. (2018). Both datasets use luminosities sourced from the 2MASS extended source catalog (Jarrett et al. 2003), with corrections applied for Galactic extinction. These luminosities are further calibrated to address sky-background over-subtraction artifacts using $L_{K_{\text{corr}}} = 1.07L_K + 1.53$ as established by Scott et al. (2013). Finally, stellar masses are calculated via $\log_{10}(M_*/M_{\odot}) = 10.39 - 0.46(L_{K_{\text{corr}}} + 23)$ (van de Sande et al. 2019), where M_* is consistent with that derived by the Jeans Anisotropic Models (JAM) dynamical methodology (Cappellari et al. 2013a; Cappellari 2013).

Ellipticity ε – For ATLAS^{3D} galaxies, ellipticities within $1R_e$ are from Emsellem et al. (2011) Table B1. Among the 260 galaxies analyzed, 17 with prominent bars have ellipticity measurements specifically at $2.5 - 3R_e$ to avoid biased inner regions (Emsellem et al. 2011; Pulsoni et al. 2020). The ellipticities of MaNGA galaxies are obtained from Zhu et al. (2023), which are uniformly measured at $1R_e$.

Spin spectroscopic parameter λ_R – The spin spectroscopic parameter λ_R is calculated across different surveys using slightly varying integration areas. In the ATLAS^{3D} survey, Emsellem et al. (2011) use circular apertures with a radius of $1R_e$, whereas the MaNGA survey integrates over a half-light ellipse (Zhu et al. 2023). This ellipse covers an area equivalent to a circle of radius $1R_e$, with a semi-major axis of $R_e/\sqrt{1-\varepsilon}$. Meanwhile, we adopt elliptical apertures for all λ_R calculations in this paper.

V_{rot}/σ profiles – The V_{rot}/σ profiles for both the ATLAS^{3D} and MaNGA galaxies are calculated as the ratio of the rotation velocity $V_{\text{rot}}(R)$ (see Equation (3)) and the azimuthally averaged velocity dispersion $\sigma(R)$ at a given in elliptical radial bins (Pulsoni et al. 2020). For the ATLAS^{3D} sample, kinematic maps are adopted from Emsellem et al. (2004) and Cappellari et al. (2011a). For the MaNGA galaxies, publicly available stellar kinematics from the SDSS DR17⁵ (Abdurro'uf et al. 2022) are used. We then apply KINEMETRY⁶ to fit the velocity and

velocity dispersion fields separately, deriving radial profiles of V_{rot} and σ for these galaxies.

Inclination angle i – Inclination angles of ATLAS^{3D} and MaNGA galaxies are adopted from Cappellari et al. (2013b) and Zhu et al. (2023), respectively.

2.2. Sample selection of early-type galaxies

The ATLAS^{3D} survey selected a sample of bright ETGs with high completeness within a distance of < 42 Mpc ($z \lesssim 0.01$) and a sky declination δ satisfying $|\delta - 29^{\circ}| < 35^{\circ}$. Additionally, these galaxies were required to have an absolute K -band magnitude brighter than -21.5 mag ($M_* \gtrsim 6 \times 10^9 M_{\odot}$), and away from the dusty region near the Galaxy equatorial plane with latitude $|b| < 15^{\circ}$. ETGs were identified morphologically by excluding galaxies with visible spiral structures, resulting in a sample similar to galaxies on the red sequence (Cappellari et al. 2011a). The ATLAS^{3D} ETG sample comprises 68 elliptical galaxies and 192 lenticular galaxies. The final sample comprises 260 nearby ETGs, with their kinematic data acquired using the SAURON IFS instrument (Bacon et al. 2001) mounted on the William Herschel Telescope. The SAURON IFS has a field of view of approximately $33'' \times 41''$ and is equipped with a square microlens array of $0.94'' \times 0.94''$. For the ATLAS^{3D} galaxies, Cappellari et al. (2011a) employed a uniform analysis pipeline to analyze the spectral datacubes, adopting a minimum signal-to-noise (S/N) threshold of 40 for adaptive binning (Cappellari & Copin 2003). Stellar kinematic was extracted using the ppxf⁷ software (Cappellari & Emsellem 2004) in conjunction with the MILES⁸ stellar template library (Sánchez-Blázquez et al. 2006)

The MaNGA survey targets galaxies within a redshift range of $0.01 < z < 0.15$ and a stellar mass range of $10^9 M_{\odot}$ to $10^{12} M_{\odot}$, achieving a spatial resolution of $2.5''$. For the MaNGA sample, stellar kinematics are derived from spectral data cubes using the Data Analysis Pipeline (DAP; Belfiore et al. (2019); Westfall et al. (2019)) with a subset of the MILES stellar library (Sánchez-Blázquez et al. 2006; Falcón-Barroso et al. 2011). Prior to kinematic extraction, the spectra are Voronoi-binned (Cappellari & Copin 2003) to a target S/N of 10 to ensure reliable stellar velocity dispersion measurements. The final SDSS DR17 includes over 10,000 galaxy data cubes after the removal of non-galaxy targets. We only select datacubes with good quality⁹ ($\text{drp3qual}=1$) as determined by MaNGA's Data Reduction Pipeline (DRP; Law et al. 2016; Yan et al. 2016), and impose additional criteria: redshift $z < 0.05$ (The sample is considered to be approximately complete.) and stellar masses between $10^{10} M_{\odot}$ and $10^{11.5} M_{\odot}$. This yields a final sample of 3,100 MaNGA galaxies that is comparable with the TNG sample.

We select ETGs using the criterion $(g - r) \geq 0.05 \log_{10}(M_*/M_{\odot}) + 0.1$ mag (Pulsoni et al. 2020) and limited the sample stellar mass range to $10^{10} \leq M_* \leq 10^{11.5} M_{\odot}$, yielding 193 ATLAS^{3D} (red points) ETGs, shown in the upper panel of Figure 1. Relying solely on color for classification proves inadequate for MaNGA galaxies (blue points), as dust reddening in spiral galaxies can significantly alter their observed colors. To address this limitation, we supplement $g - r$ color cuts with morphological classifications from the MaNGA Deep Learning catalog¹⁰, which utilizes a convolutional neural net-

⁷ <https://pypi.org/project/pxxf/>

⁸ <https://research.iac.es/proyecto/miles/>

⁹ https://manga-dynpop.github.io/pages/data_access

¹⁰ https://www.sdss4.org/dr15/data_access/value-added-catalogs/?vac_id=manga-morphology-deep-learning-dr15-catalog

⁵ <https://www.sdss4.org/dr17/manga/manga-data/>

⁶ <https://www.aip.de/en/members/davor-krajnovic/kinemetry/>

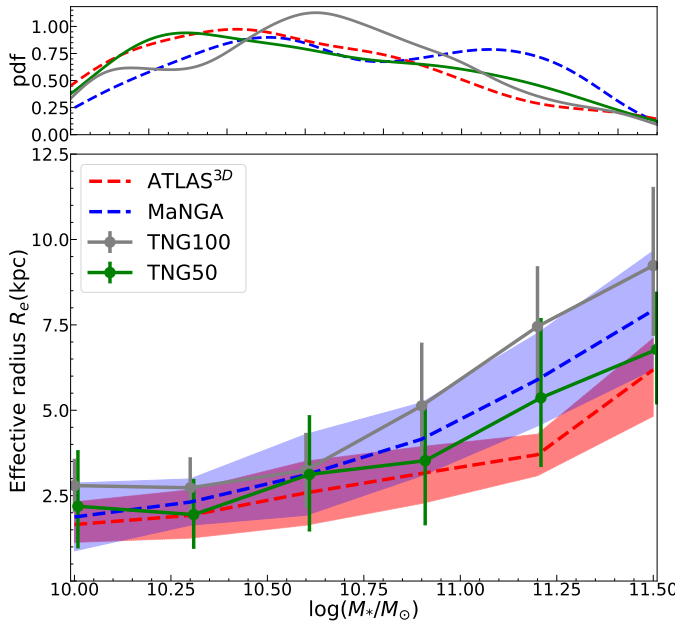


Fig. 2. Mass-size relation. *Top*: stellar mass distribution function of the chosen sample of ETGs from observational data and the TNG simulations. *Bottom*: Circularized effective radii R_e , of the selected ETG samples in the TNG100 and TNG50 simulations as a function of stellar mass, and comparison with observations (ATLAS^{3D} and MaNGA). Both TNG50 (green solid line) and TNG100 (gray solid line) galaxies share comparable stellar masses and sizes with the ATLAS^{3D} (red dashed line) and MaNGA (blue dashed line) galaxies. The lines and the points represent the median values, with colored regions and error bars indicating the range from the 16th to 84th percentile of each distribution. To avoid overlap, we shift the error bars slightly for clarity.

work trained on data from Nair & Abraham (2010). Therefore, to select ETGs from the MaNGA data, two criteria must be met simultaneously: first, these galaxies should have relatively red colors; second, they should be classified as ETGs according to the Deep Learning catalog. Adopting the methodology of Domínguez Sánchez et al. (2022), we select early-type galaxies using the same criteria. This approach identifies 599 elliptical and 334 lenticular galaxies.

3. Sample selection and mock observations of IllustrisTNG simulation galaxies

The TNG simulations use Λ CDM setup with the cosmological parameters from the Planck survey (Planck Collaboration et al. 2016), and it exploits all the advantages of the unstructured moving-mesh hydrodynamic method `Arepo`¹¹ (Springel 2010), but improves the numerical methods, the subgrid physical model, and the recipe for galaxy feedback both from stars and AGN. In particular, TNG is equipped with a novel dual mode (thermal and kinetic) AGN feedback that shapes and regulates the stellar component within massive systems, maintaining a realistic gas fraction (Weinberger et al. 2017). Also, the feedback model from galactic winds has been improved to have better representation of low- and intermediate-mass galaxies (Pillepich et al. 2018b).

The TNG suite comprises three runs using different simulation volumes and resolutions, namely TNG50, TNG100, and TNG300 (Nelson et al. 2018; Naiman et al. 2018; Marinacci

et al. 2018; Pillepich et al. 2018a, 2019; Springel et al. 2018). Each run starts at $z = 127$ using the Zeldovich approximation and evolves down to $z = 0$. In this study, we use TNG50-1 (hereafter, simply TNG50) and TNG100-1 (hereafter, simply TNG100) runs. TNG50 provides a large number of galaxies for statistical analyses and a “zoom-in”-like resolution. TNG50 includes 2×2160^3 initial resolution elements in a ~ 50 comoving Mpc box, with the baryon mass resolution of $8.5 \times 10^4 M_\odot$ and a gravitational softening radius r_{soft} for stars of about 0.3 kpc at $z = 0$. Dark matter is resolved with particles of mass $4.5 \times 10^5 M_\odot$. Meanwhile, the minimum gas softening reaches 74 comoving parsecs. TNG100 includes approximately 2×1820^3 resolution elements in a ~ 110 comoving Mpc box. The dark matter (DM) and baryonic mass resolutions of TNG100 are $m_{\text{DM}} = 7.5 \times 10^6 M_\odot$ and $m_b = 1.4 \times 10^6 M_\odot$, respectively (Springel & Hernquist 2003). The softening length employed for TNG100 for both the DM and stellar components is $\epsilon = 0.74$ kpc, while an adaptive gas gravitational softening is used, with a minimum $\epsilon_{\text{gas,min}} = 0.185$ kpc. TNG50 thus has roughly 15 times better mass resolution, and 2.5 times better spatial resolution, than TNG100 (Nelson et al. 2019).

The identification of galaxies in the simulations is performed using the Friends-of-Friends (FoF) group finding algorithm (Davis et al. 1985) and the SUBFIND algorithm (Springel et al. 2001; Dolag et al. 2009). The central galaxy (subhalo) is the first (most massive) subhalo of each FoF group, while the other galaxies within the FoF group are its satellites. All components—including gas, stars, dark matter, and black holes—that are gravitationally bound to a single galaxy are associated with their host subhalo. Each galaxy is positioned at the minimum of its respective gravitational potential well. This study utilizes galaxies from snapshot #99 (corresponding to $z = 0$) in both TNG50 and TNG100.

3.1. Sample selection of early-type galaxies

Nelson et al. (2018) showed that TNG simulations reproduce realistic galaxy colors matching SDSS observations (Strateva et al. 2001). Redder galaxies in TNG exhibit typical ETG-like properties: suppressed star formation, low gas fractions, higher metallicities, and older stellar populations. Firstly, we select all galaxies with stellar masses within the range of $10^{10.0} \leq M_* \leq 10^{11.5} M_\odot$, including both central and satellite galaxies. Then we identify ETGs using the color-mass diagram (Figure 1, lower panel), applying the same color selection criteria (dashed lines) and the same stellar mass range as we use for observations. While TNG color measurements ignore dust effects, we validated our ETG selection using a deep learning classifier (Huertas-Company et al. 2019) trained on Nair & Abraham (2010) data¹². This morphological analysis confirmed that 85% of color-selected TNG100 galaxies are genuine ETGs (1,693 E/S0 systems), with the remaining 15% being spiral galaxies. Tests show this contamination negligibly impacts our results, justifying our color-only selection approach for TNG samples.

In addition, we exclude galaxies where the effective radius R_e fell below twice the gravitational softening length ($R_e < 2r_{\text{soft}}$) where r_{soft} is 0.74 kpc and 0.288 kpc in TNG100 and TNG50, respectively. This criterion will eliminate 5 objects (2.0% of the TNG50 parent sample; $N=244$) and 245 objects (9.4% of the TNG100 parent sample; $N=2602$). We further exclude merger-contaminated galaxies through visual inspection of stellar density maps. After applying these criteria, our final ETG sample

¹¹ <https://gitlab.mpcdf.mpg.de/vrs/arepo>

¹² <https://www.tng-project.org/data/docs/specifications/#sec5r>

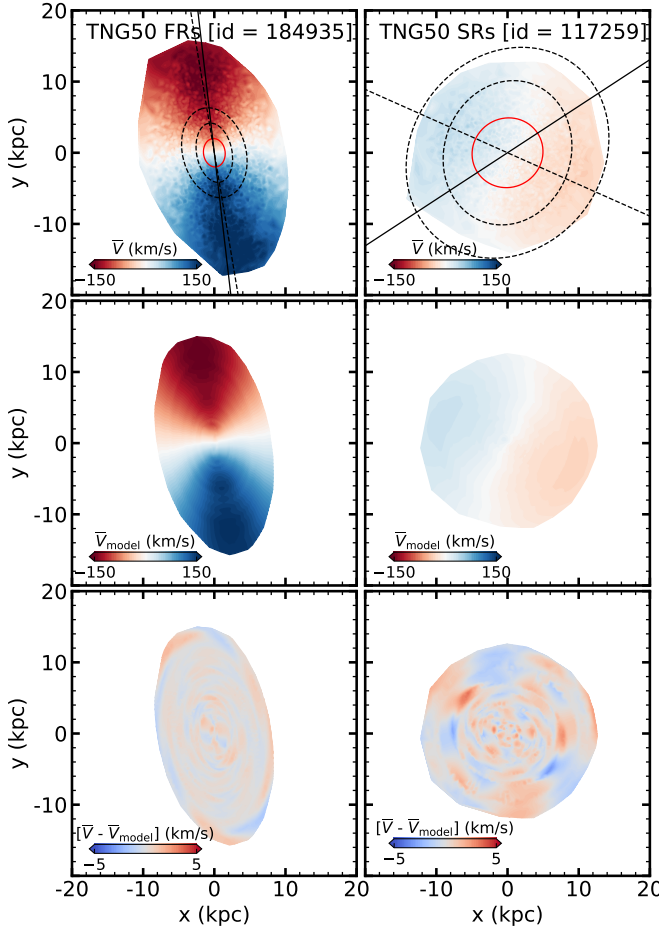


Fig. 3. Velocity maps and models of examples of a fast rotator (left) and a slow rotator (right). It shows raw data at the top, a reconstructed velocity field employing a pure cosine law along ellipses in the middle, and residuals depicting deviations at the bottom. Our visualization emphasizes structural features through isodensity ellipses spaced at regular R_e intervals from R_e to $3R_e$. The major axis orientations - with solid lines representing photometrically-derived morphological axes and dashed lines indicating kinematically-determined axes - are both measured at R_e .

consists of 2342 and 236 galaxies from TNG100 and TNG50, respectively.

The ATLAS^{3D} parent sample, which includes 260 ETGs and 611 spiral/irregular galaxies at $z \lesssim 0.01$, has been confirmed as a complete and representative sample of the nearby galaxy population, with an ETG fraction of approximately 30% (260/871) (Cappellari et al. 2011a). In the TNG simulations, our selection criteria yield ETG fractions of 27% (236/873) in TNG50 and 35% (2342/6369) in TNG100. By comparison, an observational sample (MaNGA) at $z < 0.05$ (Section 2.2) classifies 23% of galaxies as ETGs, a value closely aligned with TNG50. A separate local sample ($0.05 < z < 0.1$, $g < 16$ mag) reports a higher ETG fraction of 33% (14,034 galaxies) (Nair & Abraham 2010). TNG100 appears to reproduce a more consistent overall fraction of ETGs, while the discrepancy between TNG100 and TNG50 suggests that TNG50 may underestimate quenching efficiency. Meanwhile, in terms of spatial coverage and environmental representation, TNG50 broadly aligns with the ATLAS^{3D} survey in sampling low-density cosmological regimes (e.g., Cappellari et al. 2011b), while TNG100 corresponds to MaNGA's cosmological volume ($z < 0.05$) which incorporates higher-density

environments (e.g., Goddard et al. 2017; Greene et al. 2017). Shown in Figure 2, the stellar mass distributions of TNG50 and TNG100 galaxies show no clear differences attributable to their cosmological environments. And these environmental differences between simulation pairs do not fully account for observational-simulation discrepancies we found (see details in Section 6.3).

3.2. Mock images and data extraction

3.2.1. Mass and size

We define the total stellar mass M_* as the total bound stellar mass of the galaxy. That is, the calculation of the total stellar mass utilizes the complete set of particle data associated with galaxies and subhalos, encompassing all gravitationally bound particles identified through the SUBFIND algorithm. The effective radius R_e is estimated by the circularized effective radius in a similar way to that of observations, where the area of the ellipse that encloses half of M_* is equated to πR_e^2 .

The Multi-Gaussian Expansion (MGE) fitting is conducted using the Python package MGEFIT¹³ (Cappellari 2002) on the 2-dimensional stellar mass map within an area of $60 \text{ kpc} \times 60 \text{ kpc}$. The stellar surface density in the MGE fitting is expressed as:

$$\Sigma(x', y') = \sum_{k=1}^N \frac{\Sigma_k}{2\pi\sigma_k^2 q_k'} \exp\left[-\frac{1}{2\sigma_k^2} \left(x'^2 + \frac{y'^2}{q_k'^2}\right)\right], \quad (1)$$

where Σ_k , σ_k , and q_k' represent the total stellar mass, dispersion along the major axis, and axial ratio of the k -th Gaussian component, respectively. MGEFIT outputs the two-dimensional (2D) half-mass radius R_e and semi-major axis R_e^{maj} based on the 2D stellar mass distribution in the MGE formalism. It should be noted that the MGE approach does not extrapolate the light/density of a galaxy to infinite radii when determining R_e . Beyond three times the dispersion of the largest MGE Gaussian component, the model's flux effectively drops to zero. As a result, this method yields a slightly smaller R_e compared to other techniques (de Vaucouleurs 1948; Burstein et al. 1987; de Vaucouleurs et al. 1991). The R_e and R_e^{maj} values we use in this paper are thus scaled by a factor of 1.35, as suggested by Cappellari et al. (2013b), which subtracts potential systematic errors due to different methods.

We compare the R_e and M_* distributions of TNG galaxies with ATLAS^{3D} and MaNGA samples in Figure 2. TNG galaxies (dashed profiles) agree well with observed (solid profiles) R_e and M_* values. Those with $M_* \geq 10^{10.8} M_\odot$ may be slightly larger (~ 2 kpc), but this has minimal impact on our results. Moreover, we also examine the measurement using r -band luminosity images. It reveals that R_e measured by r -band fitting yields a slightly larger value by $\lesssim 1$ kpc than those of mass-based measurements, propagating to a marginal increase of $\Delta\lambda_R(R_e) \lesssim 0.03$. Though quantifiable, these differences negligibly impact our kinematic conclusions.

3.2.2. Kinematic maps and their Fourier expansion models

We compute the line-of-sight mean velocity and velocity dispersion fields for TNG galaxies from a randomly oriented perspective. All images are binned into 0.2 kpc intervals, equivalent to 2 arcseconds for a galaxy at a distance of 20 Mpc. This creates

¹³ Version 5.0.13, available at <https://pypi.org/project/mgefit/>

mock kinematic observations comparable to the ATLAS^{3D} survey (Cappellari et al. 2011a). Examples of fast (left panels) and slow (right panels) rotators are shown in Figure 3. Stellar particles are grouped into a regular grid centered on the galaxy, spanning a width of 40 kpc. Voronoi binning¹⁴ (Cappellari & Copin 2003) is then applied to merge bins with an insufficient number of stellar particles. Due to the Poissonian noise in particle counts, the target S/N relates to the number of particles per bin as $S/N = \sqrt{N_p}$. To achieve robust kinematics, we set $S/N \geq 10$, requiring at least 100 stellar particles per bin. The mean velocity and velocity dispersion of the i -th bin are calculated as:

$$\bar{V}_i = \frac{\sum_n M_{n,i} V_{n,i}}{\sum_n M_{n,i}}; \quad \sigma_i = \sqrt{\frac{\sum_n M_{n,i} (V_{n,i} - \bar{V}_i)^2}{\frac{N_i}{N_i-1} \sum_n M_{n,i}}} \quad (2)$$

where the index n runs over the stellar particles with mass $M_{n,i}$ within i th Voronoi bin, N_i is the particle number of this bin.

We further apply the KINEMETRY package for modeling the velocity maps through a truncated Fourier expansion along elliptical contours (Krajnović et al. 2006, 2008; Foster et al. 2016):

$$V(\psi) = V_0 + \sum_{n=1}^k [A_n \sin(n\psi) + B_n \cos(n\psi)] \quad (3)$$

where ψ denotes the eccentric anomaly, V_0 represents the systemic velocity, and A_n, B_n are the Fourier coefficients. In the case of an ideal rotating disk, symmetry requirements force all coefficients except B_1 to vanish, simplifying the velocity profile to $V(\psi) = V_0 + B_1 \cos(\psi)$. The cosine term captures the characteristic signature of regular rotation $B_1 = V_{\text{rot}}$ (the second row of Figure 3), where V_{rot} denotes the velocity amplitude, while non-zero higher-order coefficients reveal departures from axisymmetry in the velocity field (the third row of Figure 3).

4. Parameters quantifying rotation properties of galaxies

The relative importance of rotation is a key factor that determines the morphology, assembly history, and internal dynamics of galaxies. Several dimensionless parameters are commonly employed to characterize the rotational properties of galaxies, such as λ_R (the classical spin parameter), κ_{rot} (cylindrical rotation energy), and structural mass ratios derived from kinematic decomposition. Meanwhile, the higher-order term \bar{k}_5 from the Fourier decomposition of velocity fields, which is used to describe kinematic anomalies, has been used to classify fast and slow rotators in ETGs (Emsellem et al. 2004, 2011), despite lacking a well-defined physical connection to the relative importance of rotation. \bar{k}_5 is defined as the mass-weighted average of the fifth-order kinematic Fourier coefficient $k_5 = \sqrt{A_5^2 + B_5^2}/V_{\text{rot}}$ within the effective radius R_e , where V_{rot} represents the velocity amplitude, A_5 and B_5 are the fifth sine and cosine terms, respectively, in the truncated Fourier expansion for modeling the velocity field along elliptical contours (see Equation 3). The relationships among these parameters and their consistency with observational data are not yet fully understood.

This study systematically estimates and compares these parameters through: (1) rigorous evaluation of their diagnostic capabilities, (2) quantitative analysis of their inter-parameter

correlations, and (3) direct comparison with observational results. This comprehensive approach seeks to establish a universal framework for characterizing galactic rotation and classifying of slow and fast rotators of galaxies in both observations and simulations.

4.1. The λ_R - ε diagram

The spin parameter λ_R is a dimensionless parameter that quantifies the rotation of galaxies as defined by Emsellem et al. (2011)

$$\lambda_R \equiv \frac{\langle R | \bar{V} \rangle}{\langle R \sqrt{\bar{V}^2 + \sigma^2} \rangle} = \frac{\sum_i M_i R_i |\bar{V}_i|}{\sum_i M_i R_i \sqrt{\bar{V}_i^2 + \sigma_i^2}} \quad (4)$$

where the weighting with the flux is substituted here with a weighting with the mass contained within the i th Voronoi bin, M_i . R_i is the distance of the i th bin to the galaxy center. $\lambda_R(R_e)$ and $\lambda_R(3R_e)$ are computed by summing over all Voronoi bins within ellipses of one and three times R_e , with semi-major axis R_e^{maj} (Graham et al. 2018)¹⁵.

Galaxies with higher rotational velocities typically exhibit larger spin parameters (λ_R) and lower ellipticities (ε), as illustrated in the λ_R - ε diagrams of Figures 4 and 5 for both TNG simulations and IFS observations. Our analysis confirms a substantial galaxy population in the high-ellipticity region ($\varepsilon \gtrsim 0.4$) with intermediate-to-low $\lambda_R(R_e)$ values—occupying the right portion of the $\lambda_R(R_e)$ - $\varepsilon(R_e)$ plane. Pulsoni et al. (2020) argued that such galaxies ($\sim 50\%$ of total ETG samples) should be excluded as non-physical via applying an axis-ratio cut at R_e as suggested by observations (Weijmans et al. 2014; Foster et al. 2017; Li et al. 2018; Ene et al. 2018). Excluding such galaxies may induce severe selection bias. While ellipticity (ε) is commonly used to quantify inclination of galaxies, we find that these specific systems are predominantly barred galaxies, whose central $\varepsilon(R_e)$ are enhanced by the bar structure. There is no robust justification for excluding such galaxies, as the presence of elongated bar structures is unlikely to significantly alter overall galactic kinematics. To mitigate inclination errors from this central triaxiality of bars and the associated bias of excluding such galaxies, we adopt ε measured at $3R_e$. 17 of 260 galaxies from ATLAS^{3D} are measured at $2.5R_e - 3R_e$, and the majority of observational data is measured at R_e . This issue should not significantly affect our conclusion for fast-rotating cases. Emsellem et al. (2011) introduced an empirical threshold $\lambda_R(R_e) = 0.31 \sqrt{\varepsilon}$ (thin black curve in Figure 5) to distinguish fast rotators from slow rotators. This criterion is initially defined by the fifth-order kinematic Fourier coefficient \bar{k}_5 , which quantifies non-axisymmetric rotational components. For instance, the bottom-right panel of Figure 3 showcases a slow rotator with elevated \bar{k}_5 values (see details in Section 4). This classical criterion yields about 12% SRs in TNG simulations, which is consistent with the result of both ATLAS^{3D} and MaNGA.

To assess the uncertainty in kinematic measurements at different galactocentric radii, we compute the deviation between λ_R values measured within R_e and $3R_e$, as shown in Figure 6. The differences between morphologically derived position angles (PA_{morph}) and kinematically derived ones (PA_{kin}) are generally minor (By applying KINEMETRY to perform elliptical fitting on simulated galaxy images, the PA_{morph} and PA_{phot} can be derived.), i.e., < 20 degree. In contrast, $\lambda_R(R_e)$ values are

¹⁴ <https://pypi.org/project/vorbin/>

¹⁵ https://github.com/marktgraham/lambdaR_e_calc

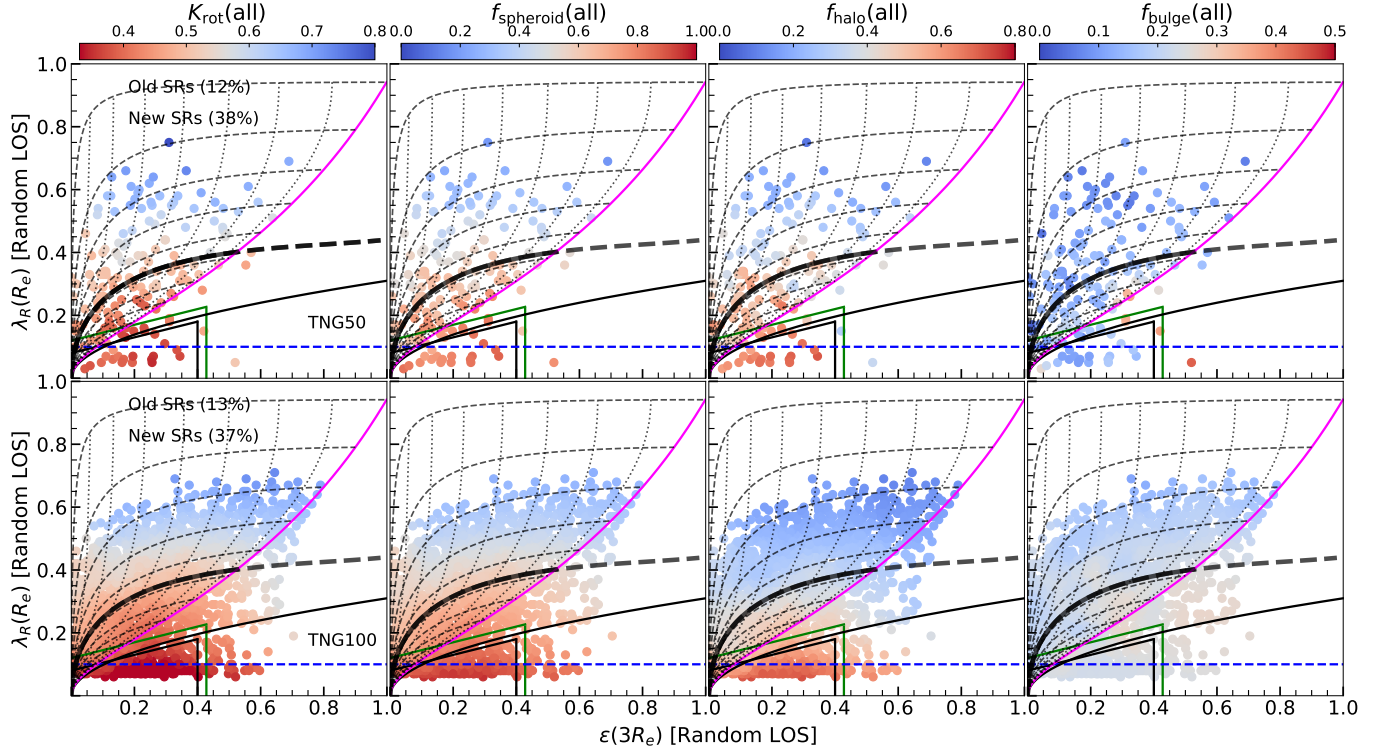


Fig. 4. The $\lambda_R(R_e) - \varepsilon(3R_e)$ diagram color coded by $\kappa_{\text{rot}}(\text{all})$, $f_{\text{spheroid}}(\text{all})$, $f_{\text{halo}}(\text{all})$, and $f_{\text{bulge}}(\text{all})$ for TNG50 (upper) and TNG100 (lower). Here, $\kappa_{\text{rot}}(\text{all})$, $f_{\text{spheroid}}(\text{all})$, $f_{\text{halo}}(\text{all})$, and $f_{\text{bulge}}(\text{all})$ represent the significance of cylindrical rotation, the spheroidal mass fraction, the stellar halo mass fraction, and the bulge mass fraction, respectively (see Section 4.3 and 4.4). The magenta curve shows the $\lambda_R - \varepsilon$ relation in edge-on view for axisymmetric galaxies derived by Cappellari et al. (2007). The black dotted curves illustrate this relation across varying i , with steps of $\Delta i = 10^\circ$. Additionally, the thin black dashed lines represent the theoretical distribution for different rotations spaced at intervals of $\Delta \lambda_{R,\text{intr}} = 0.1$. The bold black curve represents our proposed new threshold for distinguishing between SRs and FRs. This threshold is derived from the tensor virial theorem for oblate galaxies with intrinsic parameters $\lambda_{R,\text{intr}}(R_e) = 0.4$ and $\varepsilon_{\text{intr}} = 0.525$, assuming an anisotropy of $\delta = 0.7\varepsilon_{\text{intr}} = 0.367$. For comparison, the thin solid black line is the standard empirical threshold defined by $\lambda_R(R_e) = 0.31 \times \sqrt{\varepsilon}$ proposed in Emsellem et al. (2011, eq. 3). We present the proportion of SRs classified by our new threshold alongside the standard old threshold at the upper-left corner. We smooth the color data using the locally weighted regression method LOESS (Cleveland & Devlin 1988; Cappellari et al. 2013a) with a smoothing factor of 0.1. The blue horizontal dashed line represents the empirical threshold defined by $\lambda_R(R_e) = 0.1$ according to Emsellem et al. (2007), the black polygon denotes the empirical threshold set by $\lambda_R(R_e) < 0.08 + \varepsilon/4$ and $\varepsilon < 0.4$ as per Cappellari (2016), and the green polygon signifies the empirical threshold given by $\lambda_R(R_e) < \lambda_{\text{Rstart}} + \varepsilon/4$ and $\varepsilon < 0.35 + \frac{\lambda_{\text{Rstart}}}{1.538}$ (with $\lambda_{\text{Rstart}} = 0.12$ when the IFS data quality is comparable to that of SAMI) based on van de Sande et al. (2021).

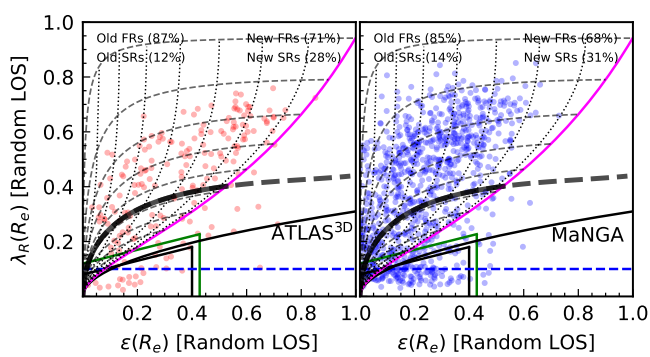


Fig. 5. The $\lambda_R(R_e) - \varepsilon(R_e)$ diagram of the sample of ATLAS^{3D} (left panel) and MaNGA (right panel). The proportions of SRs and FRs classified using our new threshold, compared to the standard old definition, are provided at the top. The definitions of all the lines are the same as those in Figure 4.

systematically lower than $\lambda_R(3R_e)$, which is expected due to the kinematic suppression often caused by central slow-rotating components, e.g., bulges. This radial dependence highlights the

importance of well-defined apertures in kinematic analyses, particularly for galaxies with structurally complex components. For consistency, we adopt $3R_e$ measurements to represent the accurate galactic properties, while R_e measurements are retained for direct comparison with observational studies.

In addition, the inclinations for the observational data are derived from the JAM modeling, which is quite time-consuming. Therefore, we then use the simple correlation $i = \arccos \sqrt{1 - \varepsilon}$ that allows us to apply our method to more IFS data where dynamical modeling is not available. we compute the deviation between i values measured within R_e and $3R_e$, as shown in the right-most panel of Figure 6. The differences between $i(3R_e)$ and $i(R_e)$ are generally minor.

4.2. Approximation of the intrinsic spin parameter $\lambda_{R,\text{intr}}$

The location of galaxies within the λ_R - ε diagram is influenced not only by their rotational properties but also by their inclination angles. To correct for this projection effect, we estimate an intrinsic spin parameter, $\lambda_{R,\text{intr}}$, which approximates the spin value for an edge-on configuration ($i = 90^\circ$), under the assumption that galaxies are axisymmetric systems. Following the method

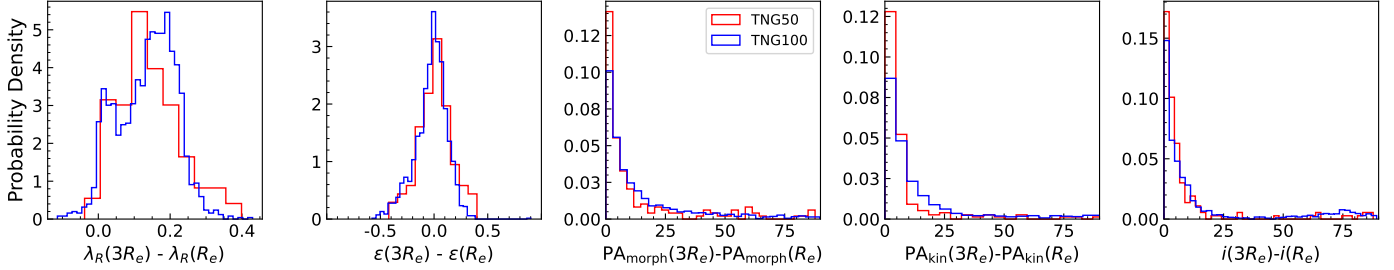


Fig. 6. The distributions of the differences between various galactic parameters measured within (at) $3R_e$ and R_e iso-density ellipses. From left to right, it depicts various galactic parameters, specifically: $\lambda_R(3R_e) - \lambda_R(R_e)$, $\epsilon(3R_e) - \epsilon(R_e)$, $PA_{\text{morph}}(3R_e) - PA_{\text{morph}}(R_e)$, and $i(3R_e) - i(R_e)$. Here, $\lambda_R(3R_e)$, $\epsilon(3R_e)$, $PA_{\text{morph}}(3R_e)$, $PA_{\text{kin}}(3R_e)$, $i(3R_e)$ represent the respective parameters measured within (at) $3R_e$, while $\lambda_R(R_e)$, $\epsilon(R_e)$, $PA_{\text{morph}}(R_e)$, $PA_{\text{kin}}(R_e)$, $i(R_e)$ denote the same parameters but measured within (at) R_e isophoto. The red and blue histograms signify the galaxies in TNG50 and TNG100, respectively.

of Binney & Tremaine (1987), we derive the edge-on (V/σ) as:

$$\left(\frac{V}{\sigma}\right)_e = \left(\frac{V}{\sigma}\right)_{\text{obs}} \frac{\sqrt{1 - \delta \cos^2 i}}{\sin i} \quad (5)$$

where the observed ratio $(\frac{V}{\sigma})_{\text{obs}} = \sqrt{\frac{\sum_j M_j \bar{V}_j}{\sum_j M_j \sigma_j^2}}$ is computed along the line-of-sight for a given inclination angle i . δ is the velocity anisotropy that is randomly sampled from a uniform distribution in the empirically-motivated range $[0, 0.7 \epsilon_{\text{intr}}]$, as suggested by Cappellari et al. (2007). We derive the edge-on ellipticity by $\epsilon_{\text{intr}} = 1 - \sqrt{1 + \epsilon(\epsilon - 2)/\sin^2 i}$. We then approximate the intrinsic spin parameter $\lambda_{R,\text{intr}}$ by the empirical formula from Emsellem et al. (2007, 2011)

$$\lambda_{R,\text{intr}} \approx \frac{a(\frac{V}{\sigma})_e}{\sqrt{1 + a^2(\frac{V}{\sigma})_e^2}} \quad (6)$$

where $a = 1.1$. $\lambda_{R,\text{intr}}$ we derive roughly corresponds to the values of λ_R projected onto the magenta curve in Figures 4 and 5.

To assess how accurately this method recovers $\lambda_{R,\text{intr}}$, we calculate the deviation $\Delta\lambda_{R,\text{intr}}$ between the intrinsic spin parameter we approximate and its real values in edge-on views, specifically for the TNG galaxies, as shown in Figure 7. The distributions for TNG50 (red histograms) and TNG100 (blue histograms) reveal no significant differences in $\lambda_{R,\text{intr}}$ measurements within R_e (left panel) versus within $3R_e$ (right panel). The results demonstrate that the method reliably recovers the intrinsic spin parameter, with deviations falling within acceptable limits.

4.3. Mass fractions of kinematically-derived structures using auto-GMM: spheroid f_{spheroid} and stellar halo f_{halo}

Recent works (Du et al. 2019, 2020, 2021) introduced auto-GMM, an automated unsupervised method for accurately decomposing galaxy kinematic structures in simulation data. This approach analyzes stellar particles in a three-dimensional kinematic phase space comprising the circularity parameter $\epsilon = j_z/j_c(e)$ (Abadi et al. 2003), the non-azimuthal angular momentum ratio $j_p/j_c(e)$, and the normalized binding energy $e/|e|_{\text{max}}$ (Doménech-Moral et al. 2012). j_z denotes the specific angular momentum component aligned with the galaxy's minor axis (z -axis) in cylindrical rotation. This quantity is normalized by $j_c(e)$, the maximum possible circular angular momentum corresponding to the particle's binding energy e . The parameter $j_z/j_c(e)$ thus

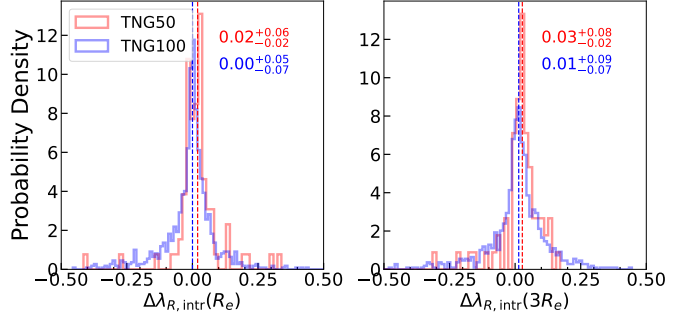


Fig. 7. The distribution of the deviation $\Delta\lambda_{R,\text{intr}}$ within different regions between the intrinsic spin parameter we approximate and its edge-on projection. *Left panel:* the distribution of the deviation $\Delta\lambda_{R,\text{intr}}(R_e)$. *Right panel:* the distribution of the deviation $\Delta\lambda_{R,\text{intr}}(3R_e)$. The red histogram signifies the galaxy sample derived from TNG50, whereas the blue histogram represents the galaxy sample from TNG100. The vertical dashed lines show the median of the intrinsic spin spectroscopic parameter estimation error. The median and the 16th and 84th percentiles are listed on the top right of each subplot.

quantifies rotation aligned with the galaxy's net angular momentum, whereas $j_p/j_c(e)$ measures misaligned rotation, and $e/|e|_{\text{max}}$ indicates how tightly bound each stellar particle is.

When applied to TNG simulations, this method successfully identified distinct structural components, including cold disk, warm disk, bulge, and stellar halo. The total spheroidal mass fraction f_{spheroid} is obtained by combining the contributions from both the bulge (f_{bulge}) and the stellar halo (f_{halo}), with data taken from Du et al. (2020) and Du et al. (2021)¹⁶. The measurements are provided at three different scales: $f(R_e)$ for stars within $1R_e$, $f(3R_e)$ within $3R_e$, and $f(\text{all})$ for all stars in each galaxy. f_{halo} defined in this way correlates closely with the strength of merger history (Du et al. 2021; Proctor et al. 2024). One of the key advantages of auto-GMM is its allowance for weakly rotating spheroids, differing from other studies (Zana et al. 2022; Cristiani et al. 2024; Liang et al. 2025) which assume zero rotation in bulges and stellar halos—a likely unrealistic assumption.

The spheroidal mass fraction f_{spheroid} serves as a quantitative measure for determining the relative dominance of spheroidal components in galaxies. Based on this metric, we can classify galaxies with $f_{\text{spheroid}} < 0.5$ as FRs which means disk structures dominate them, while those with $f_{\text{spheroid}} > 0.5$ are identified as SRs.

¹⁶ <https://www.tng-project.org/data/docs/specifications/#sec5>

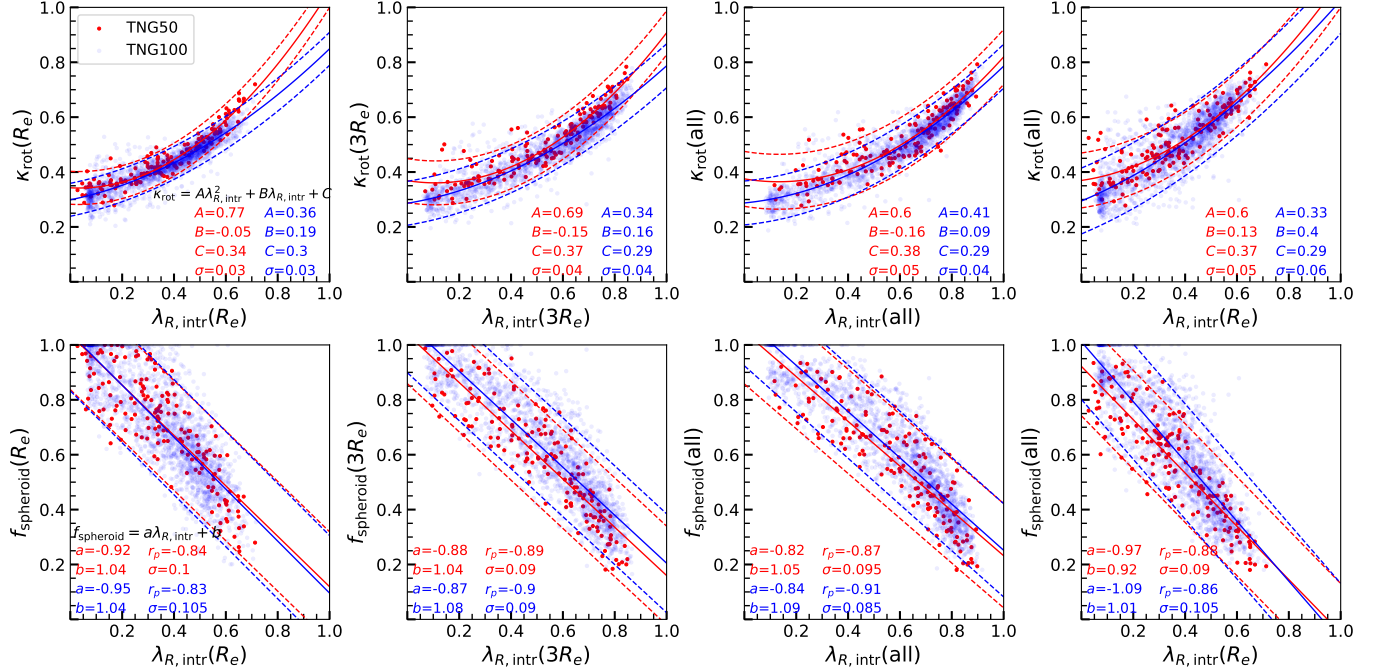


Fig. 8. The distribution and correlation of κ_{rot} vs. $\lambda_{R,\text{intr}}$ (upper) and f_{spheroid} vs. $\lambda_{R,\text{intr}}$ (lower) measured within different regions from left to right. The solid red and blue curves show the best-fit results for the TNG50 and TNG100 datasets, respectively, while the dashed curves represent their 2σ confidence interval. The corresponding fitting coefficients and σ values are listed in the bottom-right corner of each panel. In the lower panels, we additionally provide the Pearson correlation coefficient (r_p). The value of $r_p \sim -1$ indicates a strong anti-correlation between $\lambda_{R,\text{intr}}$ and f_{spheroid} .

4.4. Assessing the significance of cylindrical rotation energy κ_{rot}

The significance of cylindrical rotation is quantified by the parameter $\kappa_{\text{rot}} = \frac{K_{\text{rot}}}{K} = \frac{1}{K} \sum \left[\frac{1}{2} m_i \left(\frac{j_{z,i}}{R_i} \right)^2 \right]$, as defined in (Sales et al. 2010), where K and m represent the total kinetic energy and mass of each stellar particle, respectively. This widely-used metric provides a clear physical interpretation of ordered rotation in simulated galaxies and is computationally straightforward to evaluate.

However, several important considerations should be noted. First, while commonly adopted, the threshold of $\kappa_{\text{rot}} = 0.5$ for distinguishing between disk galaxies (corresponding to FRs) and elliptical galaxies (SRs) lacks strong theoretical justification (Zhao et al. 2020; Roshan et al. 2021; Lu et al. 2025). Second, for a completely dispersion-dominated system, theoretical considerations predict $\kappa_{\text{rot}} = 1/3$. Finally, the physical interpretation remains ambiguous for both disk-dominated galaxies ($\kappa_{\text{rot}} > 0.5$) and elliptical galaxies ($\kappa_{\text{rot}} < 0.5$). These limitations highlight the need for careful interpretation when applying κ_{rot} criteria to different galactic systems.

5. Approximating κ_{rot} and f_{spheroid} from scaling relations with $\lambda_{R,\text{intr}}$

The intrinsic spin parameter $\lambda_{R,\text{intr}}$, together with the λ - ϵ diagram, offers a relatively accessible observational metric. A higher $\lambda_{R,\text{intr}}$ value signifies that a galaxy's kinematic structure is dominated by ordered rotation, while a lower value indicates a greater influence of random motion. Consequently, Figure 4 reveals a clear trend: both f_{spheroid} and κ_{rot} decrease as $\lambda_{R,\text{intr}}$ declines. In this section, we then quantitatively examine the scaling relations connecting $\lambda_{R,\text{intr}}$, κ_{rot} , and f_{spheroid} .

We begin by investigating the relationship between $\lambda_{R,\text{intr}}$ and κ_{rot} . The fundamental difference in their velocity dependence — linear for $\lambda_{R,\text{intr}}$ versus quadratic for κ_{rot} — motivates a quadratic fitting function of the form:

$$\kappa_{\text{rot}} = A\lambda_{R,\text{intr}}^2 + B\lambda_{R,\text{intr}} + C \quad (7)$$

where A , B , and C represent the coefficients to be determined through regression analysis. This functional form naturally accommodates their distinct velocity scalings while enabling quantitative comparison of their kinematic relationship. The first row of Figure 8 reveals a robust correlation between $\lambda_{R,\text{intr}}$ and κ_{rot} (see the fitting result at the bottom-right corners). This relationship holds consistently across both TNG50 (red) and TNG100 (blue) simulations, regardless of the measurement aperture — whether considering stars within R_e , $3R_e$, or the entire system. Notably, as demonstrated in the right-most panel, $\lambda_{R,\text{intr}}(R_e)$ alone can be used to approximate the global $\kappa_{\text{rot}}(\text{all})$ with an acceptable uncertainty of ~ 0.05 , despite being measured only within the effective radius (R_e). Furthermore, the criterion $\kappa_{\text{rot}} > 0.5$ has become a standard threshold for identifying disk-dominated systems in numerical simulations, approximately equivalent to $\lambda_{R,\text{intr}}(R_e) \gtrsim 0.4$.

Our analysis further reveals a linear scaling relation between $\lambda_{R,\text{intr}}$ and f_{spheroid} , as shown in the lower panels of Figure 8. This correlation robustly validates $\lambda_{R,\text{intr}}$ as an effective diagnostic for quantifying spheroid mass fractions across different measurement apertures, see the fitting result at the bottom-right corners. The observed anti-correlation follows $f_{\text{spheroid}} \approx 1 - \lambda_{R,\text{intr}}$ (or equivalently, $f_{\text{disk}} \approx \lambda_{R,\text{intr}}$), indicating that $\lambda_{R,\text{intr}}$ directly traces disk dominance with a typical uncertainty of $\sigma \sim 0.1$. This establishes $\lambda_{R,\text{intr}}$ as a powerful observational proxy for connecting IFS kinematics to the intrinsic structural decomposition of galaxies. Even when limited to one effective radius ($\lambda_{R,\text{intr}}(R_e)$) — the typical spatial coverage of IFS observations — $\lambda_{R,\text{intr}}$ retains diagnostic power for characterizing global galaxy rotation.

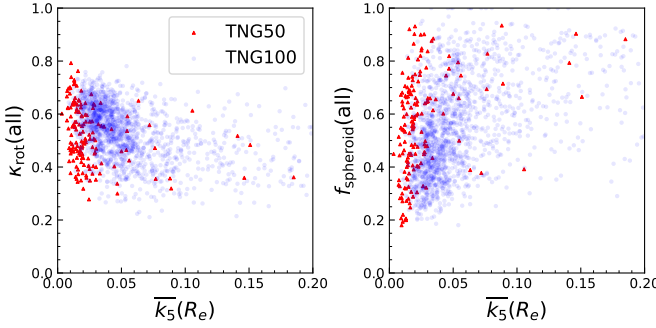


Fig. 9. $\kappa_{\text{rot}}(\text{all})$, $f_{\text{spheroid}}(\text{all})$ of the selected ETGs samples in TNG simulation, plotted as a function of $\bar{k}_5(R_e)$. No clear correlation between $\kappa_{\text{rot}}(\text{all})$ and $f_{\text{spheroid}}(\text{all})$ of the selected ETGs samples in the TNG simulations. Red and blue dots represent the samples of TNG50 and TNG100, respectively.

The parameter λ_R thus can serve as a proxy for estimating $\lambda_{R,\text{intr}}$, κ_{rot} , and f_{spheroid} . Empirically, $\lambda_{R,\text{intr}}(R_e)$ provides a reasonable approximation of the global rotational properties, specifically $\kappa_{\text{rot}}(\text{all})$ and $f_{\text{spheroid}}(\text{all})$. Moreover, it is worth highlighting that the $\lambda_{R,\text{intr}} - f_{\text{spheroid}}$ relationship is primarily determined by f_{halo} , shown in the third column of Figure 4. Bulges only contribute to scatter without altering the fundamental scaling relation, as shown in the fourth column. In the fourth column, we further leverage the empirical correlations between $\lambda_{R,\text{intr}}(R_e)$ and $\kappa_{\text{rot}}(\text{all})$, $f_{\text{spheroid}}(\text{all})$ derived from TNG50 simulations to infer approximate values of $\kappa_{\text{rot}}(\text{all})$ and $f_{\text{spheroid}}(\text{all})$ based on $\lambda_{R,\text{intr}}(R_e)$ ¹⁷ for observed galaxies. A subset of MaNGA galaxies, specifically nine randomly selected sample galaxies, has their detailed information listed in Table 1. The complete content of MaNGA, ATLAS^{3D}, TNG50, and TNG100 data is publicly available.

6. Kinematic classification of galaxies into fast (disk) and slow (elliptical) rotating galaxies

In this study, we equate disk galaxies with FRs and elliptical galaxies with SRs. Regarding this, it should be noted that morphological classifications (disk vs. elliptical galaxies) and kinematic classifications (FRs vs. SRs) describe fundamentally distinct galaxy properties. Disks and ellipticals denote visual structures observed photometrically (e.g., spiral arms vs. smooth ellipsoids; Hubble 1926, 1936; Sandage 2005), while FRs and SRs categorize galaxies based on dynamical properties quantified by spin parameter λ_R (Emsellem et al. 2007; Cappellari 2016). Historically, these classifications correlated strongly—ellipticals were presumed pressure-supported SRs, while disks were rotationally dominated FRs—driving early unification in literature. However, IFS surveys like ATLAS^{3D}, SAMI, CALIFA and MaNGA have revealed significant exceptions: part of morphological ellipticals exhibit FR kinematics (Emsellem et al. 2011; Fogarty et al. 2015), and a minority of disks show SR-like suppression of rotation (Falcón-Barroso et al. 2015; Graham et al. 2018). Thus, equating disks/ellipticals directly with FRs/SRs overlooks dynamically complex populations and risks oversimplification.

Therefore, this work introduces unified classification thresholds that reconcile galaxy morphology and kinematics (see Section 6.2). Our criteria reclassify approximately 4% of previously

Table 1. Table with main properties of 933 MaNGA galaxies used in this paper.

Plate-IFU (1)	i (2)	ε (3)	$\lambda_R(R_e)$ (4)	$\lambda_{R,\text{intr}}(R_e)$ (5)	$\kappa_{\text{rot}}(\text{all})$ (6)	$f_{\text{spheroid}}(\text{all})$ (7)
8329-1901	32°	0.12	0.46	0.63	0.68	0.30
8319-1901	33°	0.07	0.46	0.66	0.69	0.28
8243-6102	32°	0.15	0.52	0.66	0.70	0.28
8243-3701	71°	0.24	0.22	0.23	0.39	0.69
8243-6104	38°	0.22	0.16	nan	nan	nan
8243-3703	80°	0.01	0.49	0.50	0.57	0.43
8439-3702	87°	0.53	0.71	0.71	0.74	0.22
8326-1901	47°	0.18	0.57	0.67	0.70	0.27
8326-3701	34°	0.12	0.43	0.59	0.65	0.34

Notes. Column (1): The ID associated with a specific observation for a unique MaNGA galaxy. Column (2): The inclination. Column (3): The ellipticity. Column (4): The stellar spin parameter. Column (5): The intrinsic stellar spin parameter. Column (6): The significance of cylindrical rotation. Column (7) the spheroid mass fraction. For the $\lambda_{R,\text{intr}}(R_e)$ showing nan values, it means the galaxy's inclination or ellipticity is inaccurate, or the galaxy fails to meet the axisymmetric assumption, making it impossible to deduce the intrinsic ellipticity from the observed ellipticity and inclination. Among the 933 MaNGA galaxies, 97 galaxies do not have $\lambda_{R,\text{intr}}(R_e)$ as nan. Among the 193 ATLAS^{3D} galaxies, 15 galaxies have $\lambda_{R,\text{intr}}$ as nan. A complete table is available from the journal website.

identified disk galaxies as ellipticals and approximately 16% of fast rotators as slow rotators. With the associated publicly released catalog (Table 1), we establish a consistent disk/FR and elliptical/SR mapping applicable to both observational surveys and cosmological simulations.

6.1. Failure of the empirical classification of slow/fast rotators: the high-order Fourier kinematic components \bar{k}_5 and the empirical $\lambda_R(R_e) - \varepsilon$ criterion

To evaluate the reliability of the standard FRs/SRs classification in previous studies (e.g., Krajnović et al. 2011; Emsellem et al. 2011), we also calculate the \bar{k}_5 (see Section 4). However, we find that \bar{k}_5 exhibits no significant correlation with either κ_{rot} or f_{spheroid} , suggesting it poorly traces kinematic disk structure or global rotation (Figure 9), where the underlying assumption here is that galaxies with $f_{\text{spheroid}} < 0.5$ or $\kappa_{\text{rot}} > 0.5$ are classified as FRs (disk-dominated), while those with $f_{\text{spheroid}} > 0.5$ or $\kappa_{\text{rot}} < 0.5$ are classified as SRs (spheroid-dominated). This implies that both \bar{k}_5 and the standard $\lambda_R - \varepsilon$ criterion (thin black profiles in Figures 4 and 5) inadequately distinguish SRs from FRs, though they successfully identify extreme slow-rotating cases (Lu et al. 2023).

Moreover, SRs are typically identified using also other empirically derived thresholds in the $\lambda_R(R_e) - \varepsilon$ plane. Common selection criteria include: 1) Emsellem et al. (2007)'s constant threshold $\lambda_R(R_e) < 0.1$ (blue dashed line in Figure 4); 2) Emsellem et al. (2011)'s scaling relation $\lambda_R(R_e) < 0.31\sqrt{\varepsilon}$ (black curve); 3) Cappellari (2016)'s polygon criterion requiring $\lambda_R(R_e) < 0.08 + \varepsilon/4$ with $\varepsilon < 0.4$ (black polygon); and 4) van de Sande et al. (2021)'s adaptable threshold $\lambda_R(R_e) < \lambda_{R,\text{start}} + \varepsilon/4$ where $\varepsilon < 0.35 + \lambda_{R,\text{start}}/1.538$ (green polygon), adopting $\lambda_{R,\text{start}} = 0.12$ for SAMI-like data quality. Given the functional similarity of these thresholds—particularly their convergence near $\lambda_R(R_e) = 0.31\sqrt{\varepsilon}$ —we designate the Emsellem et al. (2011) relation as our reference criterion for distinguishing classical fast rotators from slow rotators. A revised threshold,

¹⁷ The catalog is publicly available.

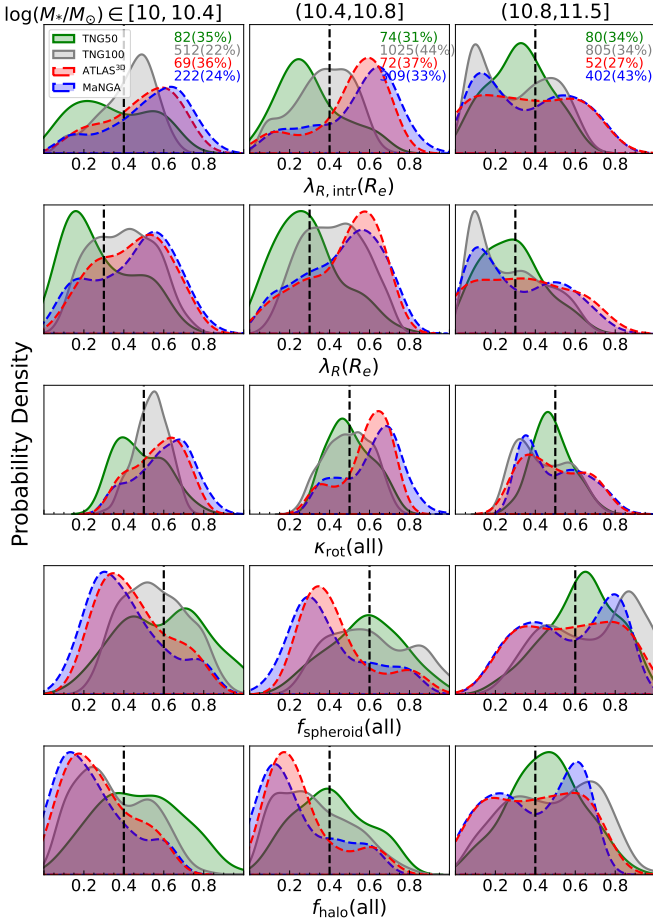


Fig. 10. The probability density distributions of $\lambda_{R,\text{intr}}(R_e)$, $\lambda_R(R_e)$, $\kappa_{\text{rot}}(\text{all})$, $f_{\text{spheroid}}(\text{all})$, and $f_{\text{halo}}(\text{all})$. The green solid, gray solid, blue dashed, and red dashed profiles represent ETG samples of TNG50, TNG100, MaNGA, and ATLAS^{3D}, respectively. The panels display three stellar mass ranges of $10^{10} - 10^{10.4} M_\odot$, $10^{10.4} - 10^{10.8} M_\odot$, and $10^{10.8} - 10^{11.5} M_\odot$, arranged from left to right. In the top right corner of each upper panel, we give the proportion and absolute count of galaxies within each mass range relative to the total ETG sample. From top to bottom, these vertical black dashed lines represent $\lambda_{R,\text{intr}}(R_e) = 0.4$, $\lambda_R(R_e) = 0.3$, $\kappa_{\text{rot}}(\text{all}) = 0.5$, $f_{\text{spheroid}}(\text{all}) = 0.6$, and $f_{\text{halo}}(\text{all}) = 0.4$, respectively.

better quantifying galactic rotation, is needed to reliably classify SRs in observations and enable robust comparisons with simulations.

6.2. Reclassification of fast and slow rotators through the kinematic bimodality

As established in the Section 5, $\lambda_{R,\text{intr}}$ exhibits strong correlations with both f_{spheroid} and κ_{rot} , confirming its utility as a fundamental parameter for characterizing galactic rotation and classifying slow versus fast rotators.

Figure 10 shows a pronounced bimodality in kinematic properties, with well-separated peaks for fast and slow rotators. Both the ATLAS^{3D} and MaNGA surveys exhibit this dichotomy:

- Fast rotators (FRs) / disk galaxies are characterized by high intrinsic spin ($\lambda_{R,\text{intr}}(R_e) \sim 0.7$), thus strong rotational support ($\kappa_{\text{rot}} \sim 0.7$) and low spheroid fractions ($f_{\text{spheroid}} \sim 0.3$).

- Slow rotators (SRs) / elliptical galaxies have low spin ($\lambda_{R,\text{intr}}(R_e) \sim 0.2$), weak rotation ($\kappa_{\text{rot}} \sim 0.3$), and dominant spheroid components ($f_{\text{spheroid}} \sim 0.8$).

The vertical black dashed lines in Figure 10 mark the new thresholds we suggest for distinguishing slow and fast rotators, giving $\lambda_{R,\text{intr}} \sim 0.4$, $\kappa_{\text{rot}} \sim 0.5$, and $f_{\text{spheroid}} \sim 0.6$. These thresholds roughly correspond to the minimum probability of the bimodal distributions. The threshold $\lambda_{R,\text{intr}} \sim 0.4$ is exactly same to that suggested by Wang et al. (2024). This bimodal distribution persists across all mass ranges, revealing a significant population of rapidly rotating ETGs. Notably, the $\kappa_{\text{rot}} \sim 0.5$ threshold – commonly used in simulations to select disk galaxies – proves observationally robust for identifying fast rotators and disk galaxies. We maintain the conventional designations of slow and fast rotators but introduce refined kinematic thresholds to better distinguish between these populations. This update ensures consistency with established nomenclature while improving the physical accuracy of the classification scheme.

The distribution of spin parameter (λ_R) is shown in the second row of Figure 10. As λ_R constitutes the projected counterpart of intrinsic $\lambda_{R,\text{intr}}$, it follows that $\lambda_R \sim \lambda_{R,\text{intr}} \sin i$ when assuming the galaxy as an isotropic thin disk (see Equation 6). This systematic projection effect depresses observed λ_R values below their intrinsic values. For fast rotators, the peak shifts from an intrinsic value of $\lambda_{R,\text{intr}} \sim 0.65$ to a lower observed value near $\lambda_R \sim 0.55$. The threshold decreases to 0.3. It further weakens the bimodality in the distribution and reduces the diagnostic power of λ_R alone, making it less accurate than $\lambda_{R,\text{intr}}$ for distinguishing between fast and slow rotators. Furthermore, van de Sande et al. (2021) selected ETGs in the SAMI Galaxy Survey using visual morphology, reporting a similarly bimodal distribution of λ_{R_e} values. As shown in their Figure 8, these bimodality peaks occur near $\lambda_R(R_e) \sim 0.5$ and $\lambda_R(R_e) \sim 0.1$ within a comparable stellar mass range to our sample – a result consistent with our findings from both MaNGA and ATLAS^{3D}.

Figure 10 clearly shows a distinct population divergence between FRs classified according to our new threshold (thick black solid profiles in Figure 4) and those identified using the conventional criterion (thin black solid profiles in Figure 4). Under the previous classification scheme, only galaxies with minimal disk components and weak rotational support—specifically elliptical systems meeting the conditions $\kappa_{\text{rot}} < 0.4$, $f_{\text{spheroid}} > 0.8$, and $f_{\text{halo}} > 0.6$ —were categorized as SRs. The TNG simulations exhibit approximately 10% more SRs compared to observational samples. Nevertheless, the overall fraction of SRs in TNG remains consistent with those derived from both the ATLAS^{3D} and MaNGA surveys. Moreover, the proposed threshold offers a universal criterion for classifying galaxies of all types—including both early-type and late-type galaxies—based on their rotational properties.

6.3. Kinematic bimodality deficiency in TNG: Systematic under-rotation of simulated ETGs

While the TNG simulations reproduce a similar overall proportion of SRs to observations—as detailed in Section 6.2—they exhibit a less distinct kinematic bimodality. This discrepancy arises from an overabundance of galaxies with intermediate rotational support, as shown in Figure 10. Both TNG50 and TNG100 show a significant deficit of fast rotators, leading to a systematic shift toward lower intrinsic spin parameter ($\lambda_{R,\text{intr}}$) values throughout the simulated population. This deficiency of fast-rotating ETGs in TNG simulations results in systematically different kinematic

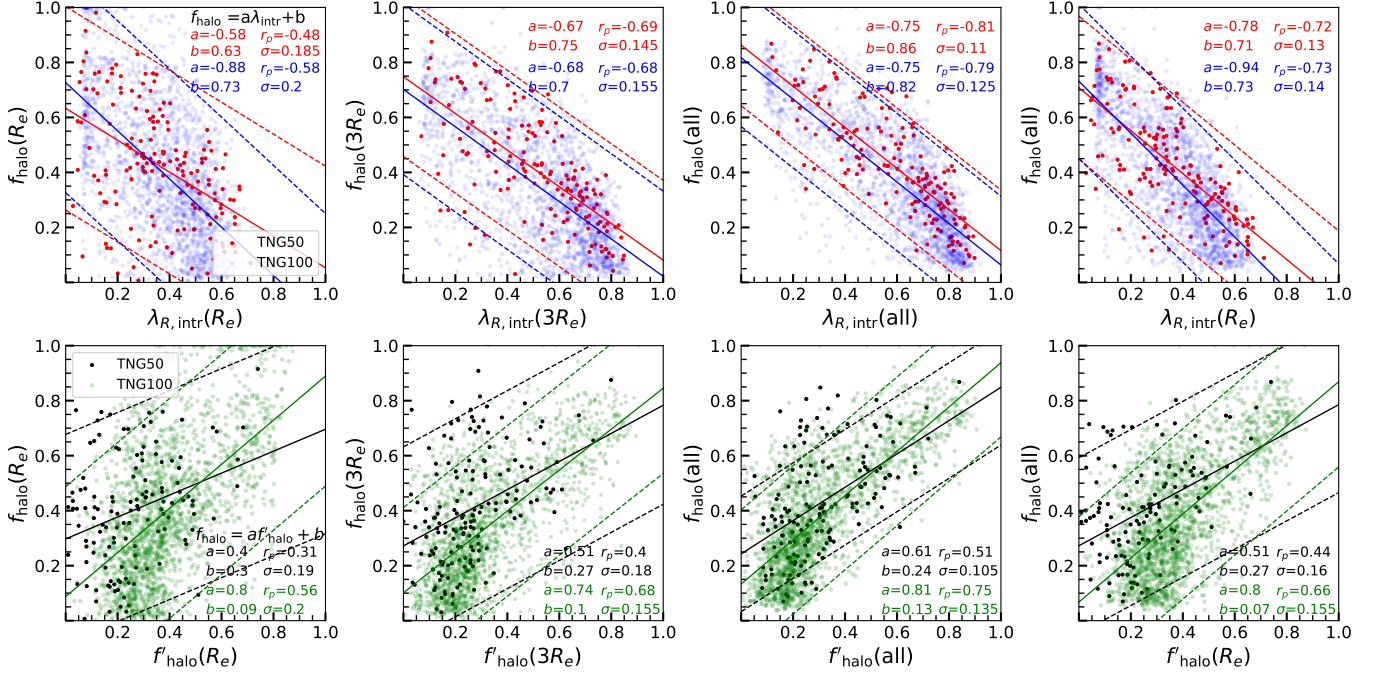


Fig. 11. Correlations of $\lambda_{R,\text{intr}}$ versus f_{halo} and f'_{halo} versus f_{halo} . The first row presents the relationships between $\lambda_{R,\text{intr}}$ and f_{halo} measured within R_e (first column), $3R_e$ (second column), and for all stars (third column). The fourth column shows the relation between $\lambda_{R,\text{intr}}(R_e)$ and $f_{\text{halo}}(\text{all})$. Solid red and blue lines, along with their corresponding dashed lines, represent the linear fits and 2σ confidence interval for the TNG50 and TNG100 datasets, respectively. Fit coefficients, σ values, and Pearson correlation coefficients (r_p) are provided in the top-right corner of each panel. The second row follows a similar layout but illustrates the relationship between f'_{halo} and f_{halo} . In this row, solid black and green lines, with accompanying dashed lines, indicate the linear fits and 2σ confidence interval for the TNG50 and TNG100 datasets, respectively.

properties compared to observations: simulated ETGs exhibit weaker rotation (lower κ_{rot}), higher spheroid fractions (f_{spheroid}), and higher stellar halo fractions (f_{halo}), as shown in Figure 10. This result manifests two primary shortcomings: (1) a near-total absence of rapidly rotating systems with $\lambda_{R,\text{intr}} > 0.6$, and (2) a displacement of the characteristic $\lambda_{R,\text{intr}}$ peak from the observed value of ~ 0.7 to below 0.5. Correspondingly, the simulations contain an overabundance of slow-rotating ETGs and yield a higher fraction of ETGs with significant spheroidal components ($f_{\text{spheroid}} > 0.5$), many of which represent disk galaxies embedded within massive stellar halos (He et al. 2025).

It is worth highlighting that the ATLAS^{3D} survey contains approximately 16% fewer massive galaxies compared to MaNGA (27% vs. 43%), as evidenced by the sparse population in the top-right corner of Figure 10 and the stellar mass distribution shown in Figure 2 (top panels). This disparity likely reflects MaNGA’s selection bias toward more massive systems, but this issue has no clear effect on the kinematic bimodality, as shown in Figure 10. TNG100 and TNG50 reproduces the ATLAS^{3D} mass distribution reasonably well, though TNG100 slightly overproduces galaxies in the $10^{10.4} - 10^{10.8} M_{\odot}$ range and underrepresents the less massive ETGs. The less pronounced kinematic bimodality is thus unlikely to be caused by the discrepancy of the proportion of ETGs within each mass range relative to the total ETG sample.

This systematic discrepancy suggests that TNG simulations produce galaxies with higher spheroid and stellar halo mass fractions than those observed. It is still unclear what reasons cause this difference. It may stem from an insufficient numerical resolution to accurately capture structural properties and their dynamical evolution, particularly in central regions, such as bars, gas inflows, and other nuclear fast-rotating structures. Further-

more, the treatment approaches of the interstellar medium and feedback subgrid models also have an impact on the kinematics in especially the inner regions of galaxies. Active galactic nucleus and stellar feedback shape the star formation history and even kinematic features via regulating gas cooling and quenching (Weinberger et al. 2018; Donnari et al. 2021). Although TNG simulations successfully reproduce many galactic properties, accurately matching observed kinematic distributions remains challenging. It is also important to note that observational IFU measurements are typically limited to central regions (within approximately R_e), which cannot fully represent the overall rotational characteristics of galaxies and introduce significant uncertainties. Consequently, the apparent bimodality observed in kinematic distributions may also be subject to reliability concerns. Moreover, as mentioned in Section 3.1, TNG50 appears to produce a smaller proportion of ETGs (27%) compared to observations (33%), this result also indicates that disk galaxies in TNG simulations exhibit lower quenching probabilities into early-type morphologies compared to observations. Consequently, in the real universe, systems with significant disk components appear more susceptible to quenching processes that transform them into ETGs—a transition that current simulations may not fully capture.

6.4. A novel method for approximating stellar halo mass fractions using $\lambda_{R,\text{intr}}$

The ubiquitous presence of massive stellar halos fundamentally challenges conventional galaxy classification and structural decomposition methods (Gadotti & Sánchez-Janssen 2012; Du et al. 2020; He et al. 2025). These halos primarily form through merger-driven processes—particularly major mergers

and strong tidal interactions—which efficiently disrupt the disks of both progenitor and satellite galaxies (Du et al. 2021). In halo-embedded disk systems, also called Sombrero-like galaxies, where low-mass disks are embedded within massive stellar halos, traditional morphological analyses often misclassify halo mass as part of the disk structure (Du et al. 2020; He et al. 2025), leading to systematic underestimation. While classical bulges have served as historical proxies for merger activity (e.g., Toomre 1977; Aguerri et al. 2001), TNG simulations demonstrate their inadequacy in capturing the full scope of merger histories (Du et al. 2021), necessitating more robust diagnostics.

Stellar halos and suppressed rotation serve as sensitive tracers of galactic merger events, as mergers dynamically convert ordered rotation into random motion, although some disk will survive from mergers with special orbital configuration (Zeng et al. 2021). This process simultaneously builds up stellar halos and erases disk kinematics. The first row of Figure 11 reveals a moderate anti-correlation between $\lambda_{R,\text{intr}}$ and the stellar halo fraction f_{halo} derived from auto-GMM analysis, though with a substantial scatter of $\sigma \sim 0.15$.

We therefore introduce a novel methodology that leverages the $\lambda_{R,\text{intr}} - f_{\text{spheroids}}$ relation established in Section 5 to estimate stellar halo masses, despite the considerable associated uncertainty. Our approach computes $f'_{\text{halo}} = f_{\text{spheroids}} - f'_{\text{bulge}}$, where bulges are operationally defined as bright central concentrations according to classical morphological criteria (Hubble 1936; Buta 2013), without distinguishing between classical and pseudo-bulge subtypes. The bulge mass fraction f'_{bulge} is approximated by integrating the stellar surface density profile over the central 0–1 kpc region in face-on projections, while $f_{\text{spheroids}}$ is approximated using the scaling relation with $\lambda_{R,\text{intr}}$. Meanwhile, we examine that f'_{bulge} deviates further from f_{bulge} if f'_{bulge} is approximated by integrating the stellar surface density profile within the central 0–2 kpc or 0–3 kpc regions.

We anticipate improved accuracy with future IFS measurements extending to larger radii, as suggested by the second and third columns of Figure 11. It is noteworthy that currently, tracer populations such as planetary nebulae can, to a certain extent, already facilitate the extension of IFS measurements to larger radii (e.g., Pulsoni et al. 2018). f'_{halo} we obtain have a somewhat acceptable agreement with dynamically derived f_{halo} values, exhibiting a scatter of approximately $\sigma \sim 0.15$. It is worth mentioning that this method is unable to measure stellar halos with $f'_{\text{halo}} \lesssim 0.3$, where the stellar halo is too small. This method enables somewhat statistical analysis of merger histories of ETGs with massive stellar halos using IFS measurements (e.g., Huang et al. 2013; Deason et al. 2016; D’Souza & Bell 2018; Monachesi et al. 2019; Du et al. 2021; Zhu et al. 2022), overcoming limitations inherent in purely morphological identification of stellar halos.

7. Radial distribution of V_{rot}/σ in the inner regions of selected fast rotators

Fast-rotating ETGs, characterized by $\lambda_{R,\text{intr}} > 0.4$ as defined in Section 6.2, serve as ideal tracers of minimally disturbed galactic evolution (van Dokkum et al. 2015; Cappellari 2016; Wang et al. 2020; Zhu et al. 2024). Their kinematic radial profiles, relatively unaffected by major mergers or strong tidal interactions, provide critical benchmarks for studying intrinsic galaxy evolution in both simulations and observations. We thus compare the radial distribution of V_{rot}/σ in Figure 12. To systematically account for the effects of stellar mass and inclination, we cate-

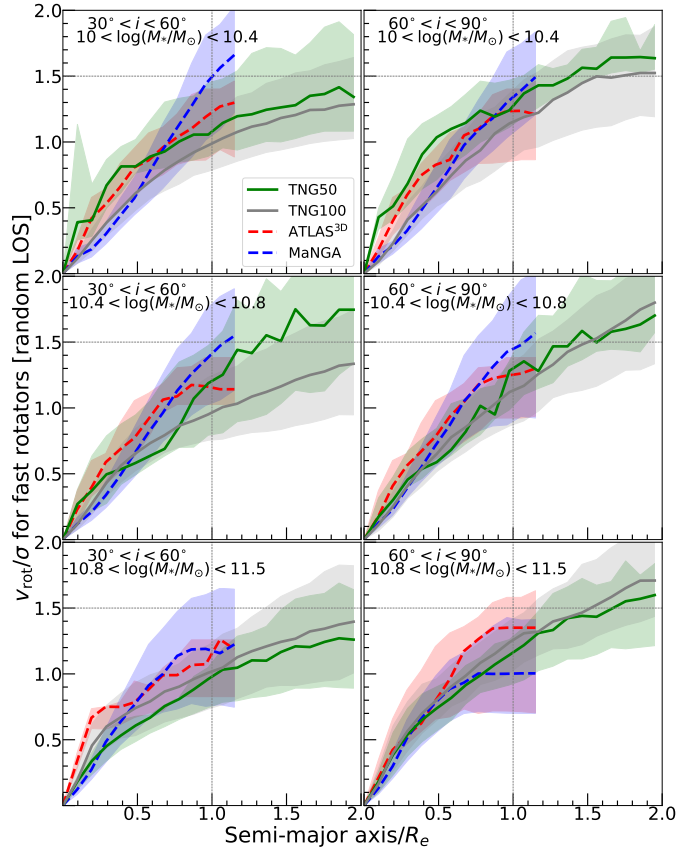


Fig. 12. Median V_{rot}/σ profiles for fast rotators selected using our new threshold ($\kappa_{\text{rot}}(\text{all}) > 0.5$), projected along a random LOS. *Top row*: it depicts galaxy samples that fall within mass ranges $[10^{10.0}, 10^{10.4}] M_{\odot}$, from left to right, galaxy samples are presented at different inclinations: $30^{\circ} - 60^{\circ}$ and $60^{\circ} - 90^{\circ}$, respectively. The green solid lines, gray solid lines, red dashed lines, and blue dashed lines, along with their corresponding shaded regions in the figure, represent the data from TNG50, TNG100, ATLAS^{3D}, and MaNGA, respectively. Both simulation’s and observation datasets showcase median profiles, with shaded regions indicating the 16th and 84th percentiles of the distribution. Vertical and horizontal dashed lines are included as visual aids for comparing simulations and observations. The profiles of simulated ETGs fast rotators closely resemble those observed. *Middle row* and *Bottom row* are the same as the *Top row*, but they depict galaxy samples that fall within mass ranges: $[10^{10.4}, 10^{10.8}] M_{\odot}$ and $[10^{10.8}, 10^{11.5}] M_{\odot}$.

gorize our galaxy sample into three mass bins from left to right. Each mass bin is further divided into two inclination subgroups, i.e., $i = 30^{\circ} - 60^{\circ}$ and $i = 60^{\circ} - 90^{\circ}$, from top to bottom. This comprehensive sampling strategy enables us to isolate fundamental kinematic trends while controlling for projection effects and mass-dependent behaviors.

We utilized KINEMETRY to separately fit the galaxy’s velocity field V and velocity dispersion field σ , to obtain the radial distributions of V_{rot} and σ for each galaxy. Figure 12 shows that the kinematic properties of fast-rotating galaxies in TNG50 (green) match reasonably well with ATLAS^{3D} galaxies. TNG100 galaxies exhibit slightly smaller V_{rot}/σ values in their central regions, likely due to enhanced numerical heating effects stemming from insufficient resolution, particularly in lower-mass systems. The MaNGA survey similarly shows somewhat depressed V_{rot}/σ ratios compared to ATLAS^{3D}, consistent with expectations given its poorer spatial resolution. Especially, the observed sharp rise in V_{rot}/σ within the central regions ($R < 0.5R_e$) of some massive ATLAS^{3D} galaxies (bottom-left panel) results

from fast-rotating structures. Moreover, it is worth highlighting that V_{rot}/σ keeps rising toward $R > R_e$, IFS kinematic measurements in $R < R_e$ clearly cannot characterize the full dynamical state of fast rotators. The potential existence of massive stellar halos around disks (Gadotti & Sánchez-Janssen 2012; He et al. 2025), for example the Sombrero galaxy, may significantly change the overall λ_R and V_{rot}/σ at large radius.

Our results indicate that the TNG simulations produce a substantially larger population of galaxies with intermediate rotational support, as detailed in Section 6.2. Although TNG50 reproduces the kinematic properties of fast-rotating ETGs—consistent with previous studies (Xu et al. 2019; Zhang et al. 2025)—it is important to note that those earlier works did not exclude the potential effect of slow rotators in their samples, a methodological choice that may obscure kinematic distinctions via inducing large scatters. It may diminish the visibility of potential discrepancies. Furthermore, differences in the inclination angles among galaxy samples can also influence the analysis. This overabundance of intermediate-rotators in TNG could explain the shallower $V_{\text{rot}}/\sigma(R)$ radial profiles reported in Pulsoni et al. (2020).

8. Discussions: evaluating kinematic analysis in advanced cosmological simulations

Similar analyses have suggested consistency between TNG simulations and observations. However, when incorporating careful prevalence estimates and inclination corrections, certain discrepancies emerge. The random orientation of galaxies may introduce non-negligible scatter in $\lambda_R - \varepsilon$ diagrams, potentially accentuating apparent simulation-observation agreement—as exemplified by the close but uncorrected alignment shown in Figure 4 and 5. The differences in probability density profiles are discernible (Figure 10, second row). A typical inclination angle i varies between 30 and 60 degrees, which reduces the spin parameter we measured along the line of sight by a factor of $\sin(i) \approx 0.5 - 0.8$. The λ_R values of fast rotators, generally within the range of 0.3 - 0.7, can thus be significantly underestimated. This geometric effect further reduces the potential kinematic discrepancies between observations and simulations. The $\lambda_R - \varepsilon$ diagram thus alone cannot conclusively establish kinematic consistency between datasets.

Our results highlight the importance of refined analyses when evaluating simulation-observation consistency for not only TNG simulations. Schulze et al. (2018), using the Magneticum Pathfinder simulation, reported general agreement in $\lambda_R(R_e) - \varepsilon$ distributions between simulated and observed ETGs. Schulze et al. (2020) further extended this approach to ~ 500 galaxies ($2 \times 10^{10} M_\odot < M_* < 1.7 \times 10^{12} M_\odot$), noting reasonable matches in two-point gradient relationships. Similar concordance was observed in EAGLE simulations by Walo-Martín et al. (2020) and van de Sande et al. (2019) ($M > 5 \times 10^9 M_\odot, z = 0$), though the latter study noted systematically lower values in Horizon-AGN and Magneticum. Our findings suggest that such comparisons may benefit from explicit treatment of projection effects to ensure conclusive interpretations.

Kinematic properties serve as a fossil record of a galaxy's formation history. Consequently, a first-order consistency between simulations and observations may be insufficient, moreover, the non-negligible mixture of slow and fast rotators in the previous classification schemes is also likely to mitigate potential discrepancy. In this study, we thus perform detailed statistical comparisons of their projection-corrected distributions across

different mass ranges within a unified quantitative framework of both simulations and observations.

9. Summary and conclusions

This study presents a comparative analysis of galaxy kinematics between the TNG simulations (TNG50 and TNG100) and observational data from the MaNGA and ATLAS^{3D} surveys. We revisit the classification of early-type galaxies into fast rotators (FRs, disk-dominated systems) and slow rotators (SRs, dispersion-supported ellipticals) using intrinsic dynamical parameters—including the intrinsic spin parameter $\lambda_{R,\text{intr}}$, rotational energy fraction κ_{rot} , and spheroid mass fraction f_{spheroid} . Our results show that widely adopted criteria, such as the empirical $\lambda_R(R_e) = 0.31 \sqrt{\varepsilon}$ relation or the Fourier harmonic coefficient \bar{k}_5 , are inadequate for robust FR/SR separation due to their weak correlation with fundamental dynamical properties. We instead propose revised thresholds ($\lambda_{R,\text{intr}} \sim 0.4$, $\kappa_{\text{rot}} \sim 0.5$, $f_{\text{spheroid}} \sim 0.6$) derived from bimodal kinematic distributions, offering a physically motivated universal distinction between rotation- and dispersion-dominated galaxies.

We also examine inter-parameter correlations among commonly used kinematic quantities and apply scaling relations derived from TNG simulations to estimate $\lambda_{R,\text{intr}}$, κ_{rot} , and f_{spheroid} in observed MaNGA and ATLAS^{3D} galaxies. Furthermore, we introduce a novel method for inferring stellar halo mass fractions from integral-field spectra (IFS) kinematic measurements, though current estimates remain subject to significant uncertainties.

Our comparison reveals a notable deficiency in the TNG simulations: they exhibit less distinct kinematic bimodality than observations, producing fewer FRs and showing systematically lower $\lambda_{R,\text{intr}}$ values. An overabundance of galaxies with intermediate rotational support and elevated spheroid or halo fractions drives this discrepancy. Although the global fractions of SRs and FRs are roughly consistent between simulations ($\sim 38\%$ SRs) and observations ($\sim 30\%$), the weakened bimodality in TNG reflects a failure to fully capture the dynamical diversity of real early-type galaxies. These findings highlight the need for improved numerical resolution and more sophisticated subgrid physics in future simulations, as well as more extensive observational constraints, to advance our understanding of galaxy formation and evolution.

10. Data Availability

Tables 1 are only available in electronic form at the CDS via anonymous ftp to cdsarc.u-strasbg.fr/130.79.128.5 or via <http://cdsweb.u-strasbg.fr/cgi-bin/qcat?J/A+A/>.

Acknowledgements. The authors gratefully acknowledge insightful discussions with Luis C. Ho, Lars Hernquist, Bitao Wang, and Ling Zhu, and also extend our heartfelt gratitude to the referee for their insightful comments, which have significantly improved the quality of the paper. This work is supported by the National Natural Science Foundation of China under grant No. 12573010, the National Key R&D Program of China (No. XY-2025-1459), the Fundamental Research Funds for the Central Universities (No. 20720230015), the Science Fund for Creative Research Groups of the National Natural Science Foundation of China (No. 12221003), and the China Manned Space Program (No. CMS-CSST-2025-A10). The TNG50/TNG100 simulation used in this work, one of the flagship runs of the IllustrisTNG project, has been run on the HazelHen Cray XC40-system at the High Performance Computing Center Stuttgart as part of project GCS-ILLU of the Gauss Centers for Supercomputing (GCS). This work is also strongly supported by the Computing Center in Xi'an, China. The authors also acknowledge the assistance of DeepSeek's AI language model in improving the language and clarity of this manuscript.

References

Abadi, M. G., Navarro, J. F., Steinmetz, M., & Eke, V. R. 2003, *ApJ*, 597, 21

Abdulr'uf, Accetta, K., Aerts, C., et al. 2022, *ApJS*, 259, 35

Aguerri, J. A. L., Balcells, M., & Peletier, R. F. 2001, *A&A*, 367, 428

Arnold, J. A., Romanowsky, A. J., Brodie, J. P., et al. 2014, *ApJ*, 791, 80

Bacon, R., Copin, Y., Monnet, G., et al. 2001, *MNRAS*, 326, 23

Belfiore, F., Westfall, K. B., Schaefer, A., et al. 2019, *AJ*, 158, 160

Binney, J. & Tremaine, S. 1987, *Galactic dynamics* (Princeton : Princeton University Press)

Blanton, M. R., Bershady, M. A., Abolfathi, B., et al. 2017, *AJ*, 154, 28

Blanton, M. R., Kazin, E., Muna, D., Weaver, B. A., & Price-Whelan, A. 2011, *AJ*, 142, 31

Blanton, M. R. & Roweis, S. 2007, *AJ*, 133, 734

Bryant, J. J., Owers, M. S., Robotham, A. S. G., et al. 2015, *MNRAS*, 447, 2857

Bundy, K., Bershady, M. A., Law, D. R., et al. 2015, *ApJ*, 798, 7

Burstein, D., Davies, R. L., Dressler, A., et al. 1987, *ApJS*, 64, 601

Buta, R. J. 2013, in *Secular Evolution of Galaxies*, ed. J. Falcón-Barroso & J. H. Knapen (Cambridge University Press), 155

Cappellari, M. 2002, *MNRAS*, 333, 400

Cappellari, M. 2013, *ApJ*, 778, L2

Cappellari, M. 2016, *ARA&A*, 54, 597

Cappellari, M. & Copin, Y. 2003, *MNRAS*, 342, 345

Cappellari, M. & Emsellem, E. 2004, *PASP*, 116, 138

Cappellari, M., Emsellem, E., Bacon, R., et al. 2007, *MNRAS*, 379, 418

Cappellari, M., Emsellem, E., Krajnović, D., et al. 2011a, *MNRAS*, 413, 813

Cappellari, M., Emsellem, E., Krajnović, D., et al. 2011b, *MNRAS*, 416, 1680

Cappellari, M., McDermid, R. M., Alatalo, K., et al. 2013a, *MNRAS*, 432, 1862

Cappellari, M., Scott, N., Alatalo, K., et al. 2013b, *MNRAS*, 432, 1709

Chabrier, G. 2003, *PASP*, 115, 763

Cleveland, W. S. & Devlin, S. J. 1988, *Journal of the American Statistical Association*, 83, 596

Crain, R. A., Schaye, J., Bower, R. G., et al. 2015, *MNRAS*, 450, 1937

Cristiani, V. A., Abadi, M. G., Taverna, A., et al. 2024, *A&A*, 692, A63

Croom, S. M., Lawrence, J. S., Bland-Hawthorn, J., et al. 2012, *MNRAS*, 421, 872

Davé, R., Anglés-Alcázar, D., Narayanan, D., et al. 2019, *MNRAS*, 486, 2827

Davis, M., Efstathiou, G., Frenk, C. S., & White, S. D. M. 1985, *ApJ*, 292, 371

de Vaucouleurs, G. 1948, *Annales d'Astrophysique*, 11, 247

de Vaucouleurs, G., de Vaucouleurs, A., Corwin, Jr., H. G., et al. 1991, *Third Reference Catalogue of Bright Galaxies*

de Zeeuw, P. T., Bureau, M., Emsellem, E., et al. 2002, *MNRAS*, 329, 513

Deason, A. J., Mao, Y.-Y., & Wechsler, R. H. 2016, *ApJ*, 821, 5

Dolag, K., Borgani, S., Murante, G., & Springel, V. 2009, *MNRAS*, 399, 497

Dolag, K., Remus, R.-S., Valenzuela, L. M., et al. 2025, *arXiv e-prints*, arXiv:2504.01061

Doménech-Moral, M., Martínez-Serrano, F. J., Domínguez-Tenreiro, R., & Serna, A. 2012, *MNRAS*, 421, 2510

Domínguez Sánchez, H., Margalef, B., Bernardi, M., & Huertas-Company, M. 2022, *MNRAS*, 509, 4024

Donnari, M., Pillepich, A., Joshi, G. D., et al. 2021, *MNRAS*, 500, 4004

D'Souza, R. & Bell, E. F. 2018, *MNRAS*, 474, 5300

Du, M., Ho, L. C., Debattista, V. P., et al. 2021, *ApJ*, 919, 135

Du, M., Ho, L. C., Debattista, V. P., et al. 2020, *ApJ*, 895, 139

Du, M., Ho, L. C., Yu, H.-R., & Debattista, V. P. 2022, *ApJ*, 937, L18

Du, M., Ho, L. C., Zhao, D., et al. 2019, *ApJ*, 884, 129

Du, M., Ma, H.-C., Zhong, W.-Y., et al. 2024, *A&A*, 686, A168

Dubois, Y., Beckmann, R., Bournaud, F., et al. 2021, *A&A*, 651, A109

Dubois, Y., Peirani, S., Pichon, C., et al. 2016, *MNRAS*, 463, 3948

Dubois, Y., Pichon, C., Welker, C., et al. 2014, *MNRAS*, 444, 1453

Emsellem, E., Cappellari, M., Krajnović, D., et al. 2011, *MNRAS*, 414, 888

Emsellem, E., Cappellari, M., Krajnović, D., et al. 2007, *MNRAS*, 379, 401

Emsellem, E., Cappellari, M., Peletier, R. F., et al. 2004, *MNRAS*, 352, 721

Ene, I., Ma, C.-P., Veale, M., et al. 2018, *MNRAS*, 479, 2810

Falcón-Barroso, J., Lyubenova, M., & van de Ven, G. 2015, in *IAU Symposium*, Vol. 311, *Galaxy Masses as Constraints of Formation Models*, ed. M. Cappellari & S. Courteau, 78–81

Falcón-Barroso, J., Sánchez-Blázquez, P., Vazdekis, A., et al. 2011, *A&A*, 532, A95

Fall, S. M. & Rodriguez-Gomez, V. 2023, *ApJ*, 949, L14

Fogarty, L. M. R., Scott, N., Owers, M. S., et al. 2015, *MNRAS*, 454, 2050

Forbes, D. A., Sippeh, L., Savorgnan, G., et al. 2017, *MNRAS*, 464, 4611

Foster, C., Pastorello, N., Roediger, J., et al. 2016, *MNRAS*, 457, 147

Foster, C., van de Sande, J., D'Eugenio, F., et al. 2017, *MNRAS*, 472, 966

Gadotti, D. A. & Sánchez-Janssen, R. 2012, *MNRAS*, 423, 877

Goddard, D., Thomas, D., Maraston, C., et al. 2017, *MNRAS*, 465, 688

Graham, A. W. & Guzmán, R. 2003, *AJ*, 125, 2936

Graham, M. T., Cappellari, M., Li, H., et al. 2018, *MNRAS*, 477, 4711

Greene, J. E., Leauthaud, A., Emsellem, E., et al. 2017, *ApJ*, 851, L33

Gunn, J. E., Siegmund, W. A., Mannery, E. J., et al. 2006, *AJ*, 131, 2332

He, W.-T., Du, M., Li, Z.-Y., & Li, Y. 2025, *A&A*, 699, A99

Huang, S., Ho, L. C., Peng, C. Y., Li, Z.-Y., & Barth, A. J. 2013, *ApJ*, 768, L28

Hubble, E. P. 1926, *ApJ*, 64, 321

Hubble, E. P. 1936, *Realm of the Nebulae*

Huertas-Company, M., Rodriguez-Gomez, V., Nelson, D., et al. 2019, *MNRAS*, 489, 1859–1879

Jarrett, T. H., Chester, T., Cutri, R., Schneider, S. E., & Huchra, J. P. 2003, *AJ*, 125, 525

Kataria, S. K. & Vivek, M. 2024, *MNRAS*, 527, 3366

Kormendy, J. 1977, *ApJ*, 218, 333

Krajnović, D., Bacon, R., Cappellari, M., et al. 2008, *MNRAS*, 390, 93

Krajnović, D., Cappellari, M., de Zeeuw, P. T., & Copin, Y. 2006, *MNRAS*, 366, 787

Krajnović, D., Emsellem, E., Cappellari, M., et al. 2011, *MNRAS*, 414, 2923

Lagos, C. d. P., Theuns, T., Stevens, A. R. H., et al. 2017, *MNRAS*, 464, 3850

Law, D. R., Cherinka, B., Yan, R., et al. 2016, *ApJ*, 152, 83

Li, H., Mao, S., Cappellari, M., et al. 2018, *ApJ*, 863, L19

Liang, J., Jiang, F., Mo, H., et al. 2025, *MNRAS*, 541, 2304

Lu, S., Du, M., & Debattista, V. P. 2025, *A&A*, 697, A236

Lu, S., Zhu, K., Cappellari, M., et al. 2023, *MNRAS*, 526, 1022

Ma, C.-P., Greene, J. E., McConnell, N., et al. 2014, *ApJ*, 795, 158

Ma, H.-C., Du, M., Ho, L. C., Sheng, M.-J., & Liao, S. 2024, *A&A*, 689, A293

Makarov, D., Prugniel, P., Terekhová, N., Courtois, H., & Vauglin, I. 2014, *A&A*, 570, A13

Marinacci, F., Vogelsberger, M., Pakmor, R., et al. 2018, *MNRAS*, 480, 5113

Monachesi, A., Gómez, F. A., Grand, R. J. J., et al. 2019, *MNRAS*, 485, 2589

Naiman, J. P., Pillepich, A., Springel, V., et al. 2018, *MNRAS*, 477, 1206

Nair, P. B. & Abraham, R. G. 2010, *ApJS*, 186, 427

Nelson, D., Pillepich, A., Springel, V., et al. 2019, *MNRAS*, 490, 3234

Nelson, D., Pillepich, A., Springel, V., et al. 2018, *MNRAS*, 475, 624

Pérez-Montaña, L. E., Cervantes Sodi, B., Rodriguez-Gomez, V., Zhu, Q., & Ogiya, G. 2024, *MNRAS*, 533, 93

Pillepich, A., Nelson, D., Hernquist, L., et al. 2018a, *MNRAS*, 475, 648

Pillepich, A., Nelson, D., Springel, V., et al. 2019, *MNRAS*, 490, 3196

Pillepich, A., Springel, V., Nelson, D., et al. 2018b, *MNRAS*, 473, 4077

Planck Collaboration, Adam, R., Ade, P. A. R., et al. 2016, *A&A*, 594, A1

Proctor, K. L., Lagos, C. d. P., Ludlow, A. D., & Robotham, A. S. G. 2024, *MNRAS*, 527, 2624

Pulsoni, C., Gerhard, O., Arnaboldi, M., et al. 2018, *A&A*, 618, A94

Pulsoni, C., Gerhard, O., Arnaboldi, M., et al. 2020, *A&A*, 641, A60

Roshan, M., Ghafourian, N., Kashfi, T., et al. 2021, *MNRAS*, 508, 926

Sales, L. V., Navarro, J. F., Schaye, J., et al. 2010, *MNRAS*, 409, 1541

Sánchez, S. F., Kennicutt, R. C., Gil de Paz, A., et al. 2012, *A&A*, 538, A8

Sánchez-Blázquez, P., Peletier, R. F., Jiménez-Vicente, J., et al. 2006, *MNRAS*, 371, 703

Sandage, A. 2005, *ARA&A*, 43, 581

Sandage, A., Freeman, K. C., & Stokes, N. R. 1970, *ApJ*, 160, 831

Santucci, G., Lagos, C. d. P., Harborne, K. E., et al. 2024, *MNRAS*, 528, 2326

Schaye, J., Crain, R. A., Bower, R. G., et al. 2015, *MNRAS*, 446, 521

Schulze, F., Remus, R.-S., Dolag, K., et al. 2020, *MNRAS*, 493, 3778

Schulze, F., Remus, R.-S., Dolag, K., et al. 2018, *MNRAS*, 480, 4636

Schwarzschild, M. 1979, *ApJ*, 232, 236

Scott, N., Graham, A. W., & Schombert, J. 2013, *ApJ*, 768, 76

Springel, V. 2010, *MNRAS*, 401, 791

Springel, V. & Hernquist, L. 2003, *MNRAS*, 339, 289

Springel, V., Pakmor, R., Pillepich, A., et al. 2018, *MNRAS*, 475, 676

Springel, V., White, M., & Hernquist, L. 2001, *ApJ*, 549, 681

Strateva, I., Ivezic, Z., Knapp, G. R., et al. 2001, *AJ*, 122, 1861

Toomre, A. 1977, in *Evolution of Galaxies and Stellar Populations*, ed. B. M. Tinsley & R. B. G. Larson, D. Campbell, 401

Valluri, M., Merritt, D., & Emsellem, E. 2004, *ApJ*, 602, 66

van de Sande, J., Lagos, C. d. P., Welker, C., et al. 2019, *MNRAS*, 484, 869

van de Sande, J., Vaughan, S. P., Cortese, L., et al. 2021, *MNRAS*, 505, 3078

van den Bergh, S. 1976, *ApJ*, 206, 883

van den Bergh, S. 1999, *European Journal of Physics*, 20, 125

van den Bosch, R. C. E., van de Ven, G., Verolme, E. K., Cappellari, M., & de Zeeuw, P. T. 2008, *MNRAS*, 385, 647

van Dokkum, P. G., Nelson, E. J., Franx, M., et al. 2015, *ApJ*, 813, 23

Walo-Martín, D., Falcón-Barroso, J., Dalla Vecchia, C., Pérez, I., & Negri, A. 2020, *MNRAS*, 494, 5652

Wang, B., Cappellari, M., Peng, Y., & Graham, M. 2020, *MNRAS*, 495, 1958

Wang, B., Peng, Y., & Cappellari, M. 2024, *Nature Astronomy*

Weijmans, A.-M., de Zeeuw, P. T., Emsellem, E., et al. 2014, *MNRAS*, 444, 3340

Weinberger, R., Springel, V., Hernquist, L., et al. 2017, *MNRAS*, 465, 3291

Weinberger, R., Springel, V., Pakmor, R., et al. 2018, *MNRAS*, 479, 4056

Westfall, K. B., Cappellari, M., Bershady, M. A., et al. 2019, *AJ*, 158, 231

Xu, D., Zhu, L., Grand, R., et al. 2019, *MNRAS*, 489, 842–854

Yan, R., Bundy, K., Law, D. R., et al. 2016, *AJ*, 152, 197

York, D. G., Adelman, J., Anderson, Jr., J. E., et al. 2000, *AJ*, 120, 1579

Yun, K., Pillepich, A., Zinger, E., et al. 2019, *MNRAS*, 483, 1042

Zana, T., Lupi, A., Bonetti, M., et al. 2022, *MNRAS*, 515, 1524

Zeng, G., Wang, L., & Gao, L. 2021, *MNRAS*, 507, 3301

Zhang, L., Zhu, L., Pillepich, A., et al. 2025, *A&A*, 699, A320

Zhao, D., Du, M., Ho, L. C., Debattista, V. P., & Shi, J. 2020, *ApJ*, 904, 170

Zhu, K., Lu, S., Cappellari, M., et al. 2023, *MNRAS*, 522, 6326

Zhu, K., Lu, S., Cappellari, M., et al. 2024, *MNRAS*, 527, 706

Zhu, L., Pillepich, A., van de Ven, G., et al. 2022, *A&A*, 660, A20

Zhu, L., van de Ven, G., Méndez-Abreu, J., & Obreja, Á. 2018a, *MNRAS*, 479, 945

Zhu, L., van de Ven, G., van den Bosch, R., et al. 2018b, *Nature Astronomy*, 2, 233

Zhu, L., van den Bosch, R., van de Ven, G., et al. 2018c, *MNRAS*, 473, 3000

Zhu, Q., Xu, D., Gaspari, M., et al. 2018d, *MNRAS*, 480, L18